Influence of Local Collagen Fiber Orientation and Dispersion on the Mechanical Behavior of Atherosclerotic Plaques

A Parameter Study

Master of Mechanical Engineering (BioMechanical Design)

Mobina Izadpanah

Delft University of Technology

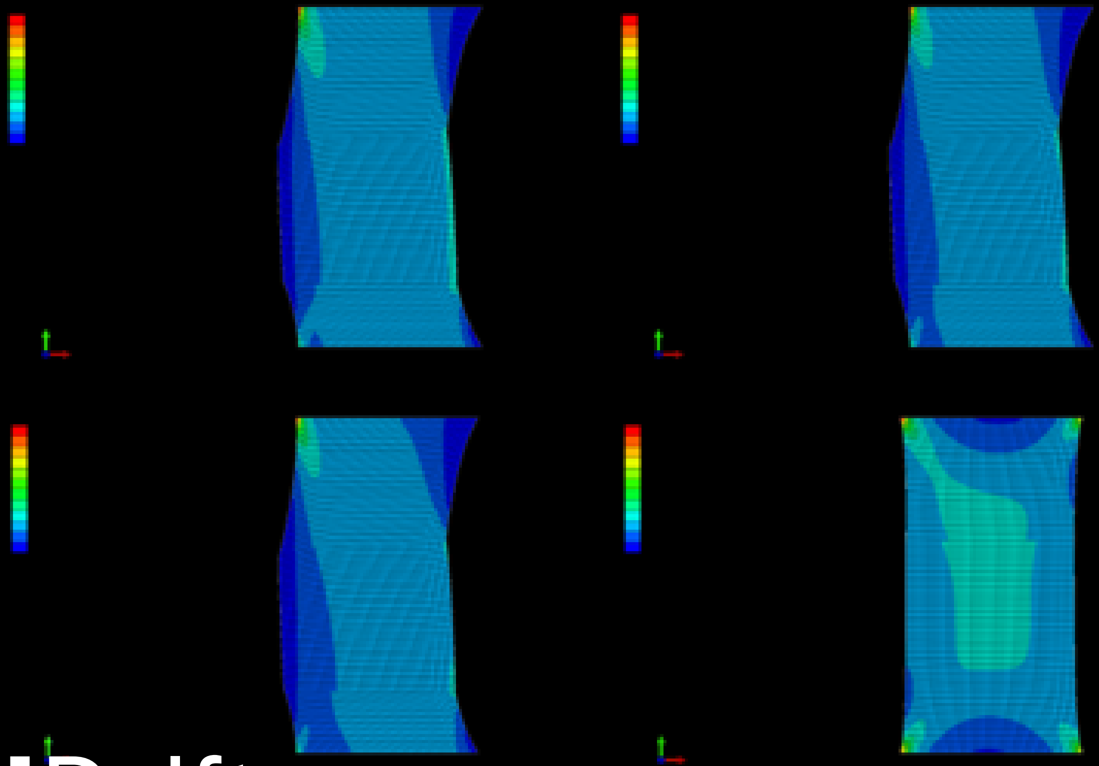

Influence of Local Collagen Fiber Orientation and Dispersion on the Mechanical Behavior of Atherosclerotic Plaques

A Parameter Study

by

Mobina Izadpanah

Supervisor:	Behrooz Fereidoonnezhad, Ali Akyildiz
Academic Year:	2023-24
Faculty:	Mechanical Engineering, Delft

Cover:	A Parameter Study on a Finite Element Model of Atherosclerotic Plaque
Style:	TU Delft Report Style, with modifications by Daan Zwaneveld

TU Delft

Preface

Working on this project has been a tremendous opportunity, and I am profoundly grateful for the experience. First and foremost, I would like to extend my heartfelt thanks to my supervisors, Ali Akyildiz and Behrooz Fereidoonnezhad, for their unwavering support, patience, and guidance throughout this journey. Their expertise and encouragement have been invaluable. I also wish to thank Yanjing Liu for her continuous support and contributions to this project. Additionally, this research builds upon the work of former master's students, Maarten Swaab and Pablo de Miguel. I am deeply appreciative of their efforts and the meticulous documentation of their results and data, which laid a solid foundation for my work. My journey to TU Delft would not have been possible without the Justus Louise van Effen Excellence Scholarship. This scholarship enabled me to attend my dream school and study in the beautiful city of Delft. I am also personally grateful to Mr. Ismail Yetim for his assistance to scholarship students, which has been instrumental in my academic pursuit. Lastly, I owe everything to my parents. Their encouragement to follow my dreams, no matter the obstacles, has been my driving force. I am forever grateful for their love and support. This work, along with everything I have achieved and will achieve, is dedicated to them.

Mobina Izadpanah
Delft, August 2024

Summary

Atherosclerotic plaque biomechanics are critical for understanding plaque stability and the risk of rupture, which can lead to severe cardiovascular events. Current modeling approaches often overlook the localized material properties of atherosclerotic plaque, leading to gaps in accurately predicting plaque behavior under physiological conditions or surgical treatments. This study aimed to address this gap by implementing local material properties of atherosclerotic plaque in a computational simulation using the Holzapfel-Gasser-Ogden (HGO) model. Three samples were modeled in the commercial software ABAQUS, and an unexpected C-shaped deformation prompted a comprehensive parameter study to investigate the influence of local and global material parameters on the plaque sample's mechanical behavior. The results indicated the vital impact of dominant fiber orientation, fiber strength, and fiber density on sample deformation, stress contribution, and its overall mechanical response.

Contents

1

Introduction

Soft fibrous materials play a vital role in biomedical research, offering valuable insights into the mechanical properties of various biological tissues such as tendons, ligaments, skin, and cardiovascular structures. A better understanding of soft biological materials is crucial for the improvement of medical interventions, surgical simulations, and artificial tissue engineering. This chapter aims to provide an introduction to the mechanical behavior of soft fibrous materials, focusing on atherosclerotic plaque, a specific cardiovascular tissue.

1.1. Background

Soft tissue is a primary group of tissue that binds, supports, and protects our human body and structures such as organs. This class of tissues is a wide-ranging biological material in which the cells are separated by extracellular material. Soft tissues may be distinguished from hard (mineralized) tissues such as bones for their high flexibility and their soft mechanical properties; and examples for soft tissues are tendons, ligaments, blood vessels, skins or articular cartilages among many others. Most soft tissues of our body are anisotropic complex fiber-reinforced composite structures. Their mechanical behavior is strongly influenced by the concentration and structural arrangement of constituents such as collagen and elastin, the hydrated matrix of proteoglycans, and the topographical site and respective function in the organism [8].

In order to describe a model for soft tissues, it is beneficial to review their general mechanical characteristic. Most soft tissues behave anisotropically because of their fibers which tend to have preferred directions. Most fibrous soft tissues exhibit a characteristic tensile stress-strain behavior, typically comprising three main phases. The tensile stress-strain behavior of skin, which is mainly composed of soft tissues, can represent the mechanical behavior of many collagenous soft tissues. In the skin's soft tissue parts, the three-dimensional network of fibers is oriented parallel to the surface, though some fibers also have out-of-plane components to prevent shearing. Figure 1.1 depicts a typical J-shaped (tensile) stress-strain curve for skin. Without load, collagen fibers, arranged in a rhombic pattern, are relaxed and appear wavy and crimped. Initially, low stress allows large deformations of individual collagen fibers without stretching them. In phase I, the tissue behaves like a soft (isotropic) rubber sheet, with elastin fibers (which keep the skin smooth) primarily responsible for stretching. The stress-strain relationship is approximately linear, with a low elastic modulus.

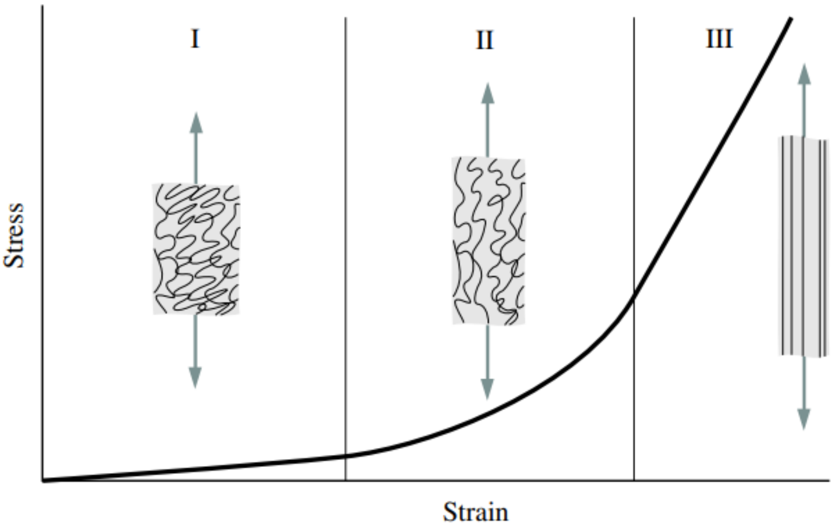

Figure 1.1: Schematic diagram of a typical (tensile) stress-strain curve for skin showing the associated collagen fiber morphology [9]

In phase II, as the load increases, collagen fibers align with the load direction and bear the load. Crimped fibers elongate and interact with the hydrated matrix. Deformation causes sequential uncrimping of fibrils. In phase III, at high tensile stresses, crimp patterns disappear, and collagen fibers straighten, aligning with the load direction. The straightened fibers resist the load strongly, making the tissue stiffer. The stress-strain relation becomes linear again. Beyond this phase, the ultimate tensile strength is reached, and fibers start to break [9].

Having established the fundamental properties and mechanical behavior of soft fibrous tissues, it is essential to consider their role in atherosclerosis, a vascular disease characterized by the accumulation of lipids. Biomechanical and biochemical mechanisms then contribute to the development of a lesion known as an atherosclerotic plaque, which is primarily composed of fibrous tissue with varying density and cellularity. A visualization of atherosclerosis is presented in Figure 1.2. Advanced atherosclerosis can lead to lesions that reduce or block the flow of oxygen-rich blood, resulting in oxygen deficiency in the tissues. Clinical emergencies, such as myocardial infarction and stroke, can occur due to plaque rupture and the subsequent release of highly thrombogenic material and lipids into the bloodstream [10]. Atherosclerosis is responsible for about 50% of deaths in Western societies, affecting the heart and brain and leading to ischemic heart disease (IHD) and ischemic stroke. IHD is the leading cause of death globally, with around 610,000 annual deaths in the U.S., while coronary heart disease alone results in over 370,000 deaths each year. Approximately 735,000 Americans experience a heart attack annually, with 75% due to plaque rupture, particularly in men over 45 and women over 50. Stroke, primarily caused by atherosclerosis, is the fifth leading cause of death and a major cause of long-term disability, with nearly 795,000 strokes and 140,323 deaths annually in the U.S. [16].

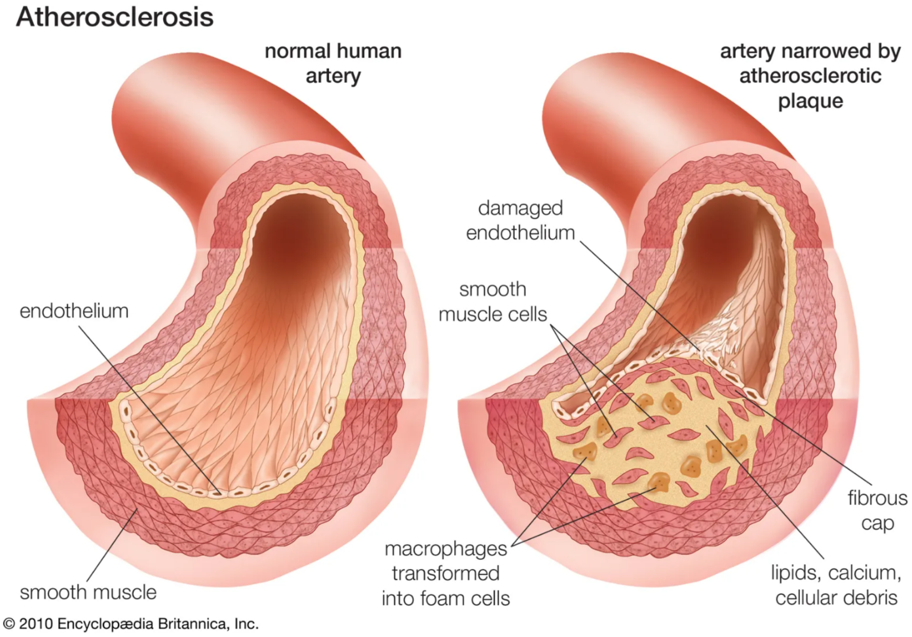

Figure 1.2: A normal artery compared with an artery affected by atherosclerosis [3].

Several surgical procedures are available to treat atherosclerosis. Coronary angioplasty involves threading a catheter through a blood vessel to the heart, where a balloon is inflated to enlarge the vessel opening and improve blood flow (Figure 1.3). Types of percutaneous coronary intervention (PCI) procedures include balloon angioplasty, where a balloon is inflated inside the blocked artery to open it; atherectomy, where a device on the end of a catheter shaves away the blockage; laser angioplasty, where a laser vaporizes the blockage; and coronary artery stent placement, where a tiny mesh coil is expanded and left inside the artery to keep it open.

Coronary artery bypass surgery, often referred to as bypass surgery, is commonly performed on individuals with angina due to coronary artery disease. It involves grafting a piece of a healthy vein from the leg or chest wall above and below the blocked area of a coronary artery, allowing blood to flow around the blockage. Multiple arteries may be bypassed during a single surgery. These treatments collectively aim to manage and alleviate the symptoms and risks associated with atherosclerosis, improving patient outcomes and quality of life [15].

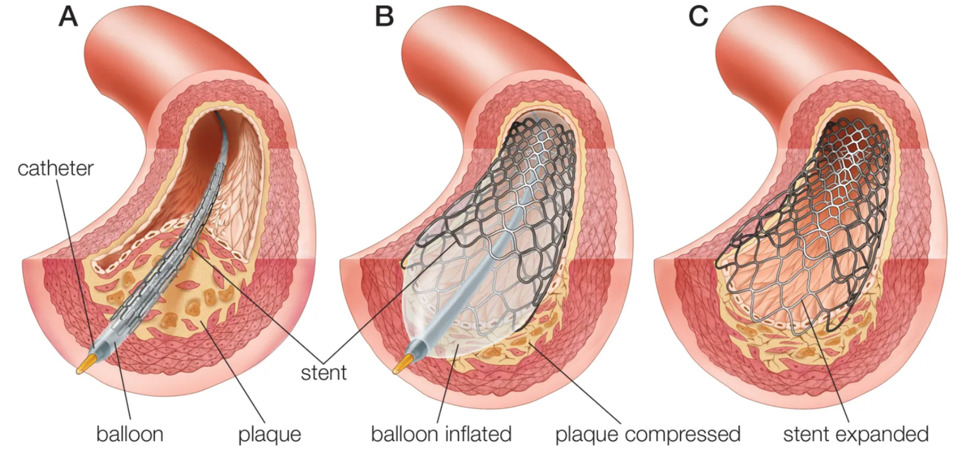

© 2010 Encyclopædia Britannica, Inc.

Figure 1.3: Balloon angioplasty and stent insertion (A) In a coronary artery where blood flow is obstructed by the growth of atherosclerotic plaque, the point of obstruction is reached by a cardiac catheter encased in an inflatable balloon and wire-mesh stent. (B) The balloon is inflated, thus expanding the stent, dilating the artery, and compressing the plaque. (C) The balloon is deflated and withdrawn with the catheter, leaving the stent expanded against the arterial wall [3].

Although surgical treatments for atherosclerosis diseases can be highly effective, they are not without limitations and carry potential complications and health risks. The complications associated with atherosclerotic surgery can vary depending on the specific procedure performed. Common potential complications include excessive bleeding at the surgical site, infection, and blood clot formation in newly opened or bypassed arteries, which may lead to a heart attack or stroke.

Understanding the structure of atherosclerotic plaque and its mechanical response to external loads can offer valuable insights into its interaction with medical devices. This knowledge can lead to the enhancement of existing surgical procedures or the development of new techniques, ultimately improving the success rate of treatments.

The mechanical behavior of atherosclerotic plaques, such as their propensity to rupture, can be linked to the underlying microstructure of collagen fibers. Current surgical treatments often lack an assessment of the plaque rupture risk. Experimental studies characterizing the failure properties of plaque tissue have primarily reported bulk mechanical properties, such as ultimate tensile failure strain and strength, under the assumption of tissue homogeneity [13, 7, 14, 17, 12]. However, fibrous plaque tissue is structurally heterogeneous, largely due to local variations in collagen fiber architecture [1]. The relationship between the mechanical failure characteristics of plaque tissue and its collagen architecture was recently investigated by Johnston et al. (2021). Their study demonstrated interplaque differences in predominant fiber orientation and reported higher ultimate stresses and lower ultimate strains for fibrous plaque cap samples with a predominantly circumferential fiber orientation [11]. Nevertheless, this study was limited to gross mechanical and structural properties [4]. Therefore, there is a gap in research on local material properties and their link to atherosclerotic plaque behavior.

In a recent experimental study by Torun et al. (2023), local collagen fiber orientation and dispersion were reported for a series of human carotid endarterectomy samples, along with the results of uniaxial tensile tests [18]. To the best of the author's knowledge, there have been no attempts to implement these local properties in finite element models to investigate their effect on mechanical behavior of plaque.

1.2. Aim of Study

This study aims to incorporate the local collagen fiber orientation and dispersion of atherosclerotic plaque into a finite element model. By utilizing the Holzapfel-Gasser-Ogden (HGO) material model, the research seeks to simulate uniaxial tensile testing to investigate the influence of these local material characteristics on the deformation and mechanical response of the tissue. Through this approach, the research endeavors to provide a deeper understanding of how the heterogeneous structure of collagen fibers within atherosclerotic plaques impacts their mechanical behavior under load, potentially informing better predictive models for plaque rupture and enhancing the development of surgical treatments.

2

Methods

The Methods chapter details the research methodology and is divided into two sections. Section 2.1 addresses the material parameters, material models, and experimental data, while Section 2.2 elaborates on the Finite Element model implemented in ABAQUS.

2.1. Material Parameters

2.1.1. Experimental Data

The experimental data used in this research were collected by Guvenir Torun et al. (2023) at Erasmus Medical Center, Rotterdam, Netherlands [18]. Eighteen human carotid endarterectomy (CEA) samples, obtained from arteries with at least 70% stenosis, were collected at Erasmus Medical Center and subsequently scanned using a micro-computed tomography scanner to identify calcified regions. Rectangular-shaped tissue strips were then prepared from the non-calcified fibrous tissue regions, with the length of the strips aligned in the circumferential direction of the artery as shown in Figure 2.1.

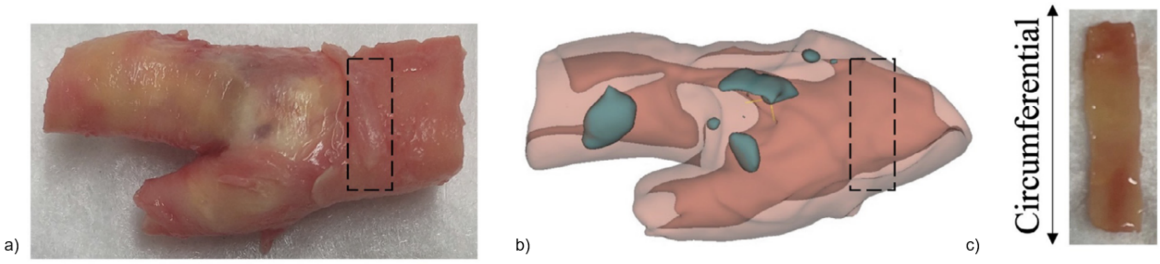

Figure 2.1: Fibrous plaque tissue sample preparation. (a) Carotid plaque sample collected in an endarterectomy (CEA) surgery. (b) 3-D plaque anatomy reconstructed from the micro-computed tomography (micro-CT) scan of the CEA sample, used to locate the calcifications within the tissue. (Calcifications are in turquoise color.) (c) A rectangular-shaped fibrous tissue strips, with the long axis aligned in the circumferential direction, obtained from a non-calcified region of the CEA sample [18].

After sample preparation, multiphoton microscopy was employed to capture the 3D collagen network of the luminal side of the CEA strips, using collecting Second Harmonic Generation (MPM-SHG) signals in the form of stacks of planar images. Rather than imaging the entire sample, the sample was divided into a grid of tiles (Figure 2.2.c). A subset of these tiles was microscopically imaged to characterize fiber properties. The fiber properties of the remaining tiles were linearly interpolated from the acquired data.

Images obtained from microscopy were analyzed by ImageJ (NIH, USA), the FOA (Fibre Orientation Analysis) tool (S. Mariën, TU/e, Netherlands.), and Fiblab (TU/e, Netherlands) resulting in calculation of isotropic fraction (P_{iso}), the predominant fiber angle (α), which is the angle of the highest number of fibers, the standard deviation (σ_p) of the fiber angle distribution, and the anisotropic fraction ($P_{ani} = 1 - P_{iso}$). As both σ_p and P_{ani} describe the dispersion of fibers, a dispersion index (DI) comprising both parameters was defined as follows

$$DI = \frac{\sigma_p}{\sigma_{max}} \times 0.5 + P_{iso} \times 0.5 \tag{2.1}$$

where σ_{max} is the standard deviation of a flat histogram (from 0 to 180 degrees), which is equal to 53. DI ranges from 0 (totally aligned fibers) to 1 (totally dispersed fibers).

Immediately after the SHG, the tissue strips were prepared for mechanical testing. Uniaxial tensile tests were carried out on 31 non-calcified CEA strips, to study their mechanical

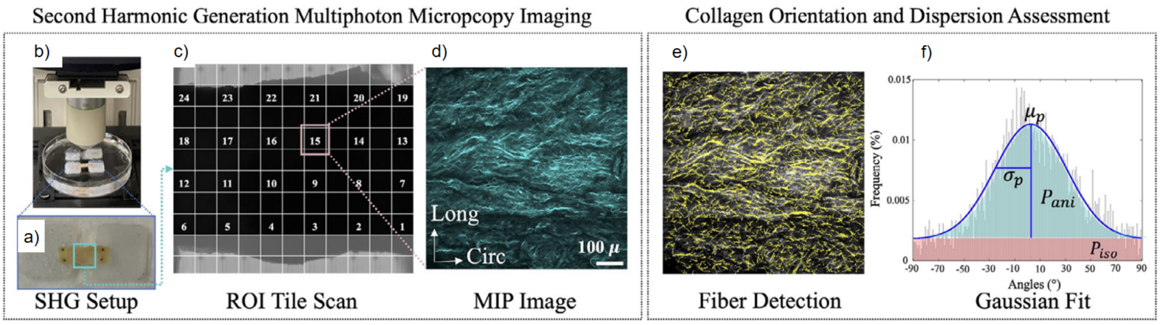

Figure 2.2: The pipeline of quantitative structural imaging of fibrillar collagen organization. (a) Test strip fixated with surgical needles to a silicone rubber cured on the glass petri dish filled with PBS. (b) Strip under the microscope. (c) ROI Tile scan per each tile performed by SHG. The imaging was performed by skipping one to two tiles between each defined tile in both circumferential and longitudinal directions (d) MIP image obtained from image stack. (e) Fiber detection by using the Fiblab Software for obtaining the histogram of detected collagen fibers. (d) Fitting Gaussian Distribution to the collagen fiber histogram to obtain α (also known as μ_p), σ_p, P_{iso} and P_{ani} parameters. (SHG: Second Harmonic Generation Multiphoton Microscopy Imaging, ROI: Region of Interest, MIP: Maximum Intensity Projection, α: the pre-dominant angle, σ_p: standard deviation, P_{iso}: isotropic fraction,P_{ani}: anisotropic fraction) [18].

response to large deformation and the rupture properties in the circumferential direction. Ultrasound imaging was performed during the process to determine the thickness of the strips. The experimental protocol consisted of three stages to generate stress-strain curves. Initially, samples were pre-stretched to a force of $0.05N$ to achieve a linear configuration. This was followed by a preconditioning phase involving ten cycles of stretching to 10% strain. Finally, samples were subjected to continuous stretching until failure. An example of this procedure and its result is presented in Figure 2.3.

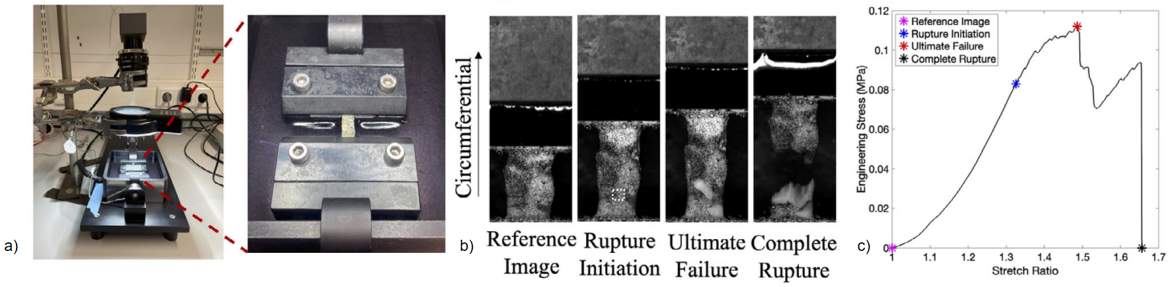

Figure 2.3: Uniaxial tensile testing until tissue failure. (a) The custom-built tensile testing setup. (b) Various stages during the uniaxial tensile testing. (c) The stages marked on the tensile stress-stretch ratio curve [18].

The results section presented data from 29 mechanical tests. Of these, six samples exhibited central rupture, while the remaining samples failed at the clamping region. Given the potential for stress concentration at the clamp sites, which can mask the influence of local material properties on failure, only the six samples with central rupture were considered for further analysis. Among these, fiber orientation and dispersion maps were generated for three samples. The dimensions of these samples are presented in Table 2.1 and the corresponding results are depicted in Figures 2.5 - 2.6. In the tiles represented in the figures, the solid lines indicate the orientation derived from experimental imaging, while the dashed lines correspond to the interpolated orientation. The color of each tile, which can be interpreted using the color bar on the left, represents the dispersion index.

Table 2.1: Sample Dimensions and Rupture Location [5]

Sample Name	Length (mm)	Width (mm)	Thickness (mm)	Rupture Location
A	7.39	4.52	0.61	Central
B	9.2	5.78	2.039	Central
C	7.98	1.99	0.52	Central

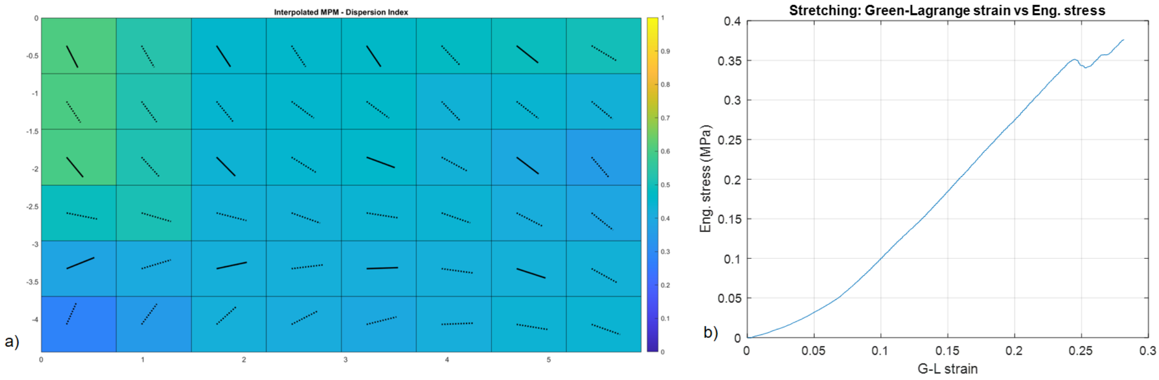

Figure 2.4: Sample A (a) Interpolation Map of Fiber Orientation and Dispersion (b) Engineering Stress-Green-Lagrange Strain [5].

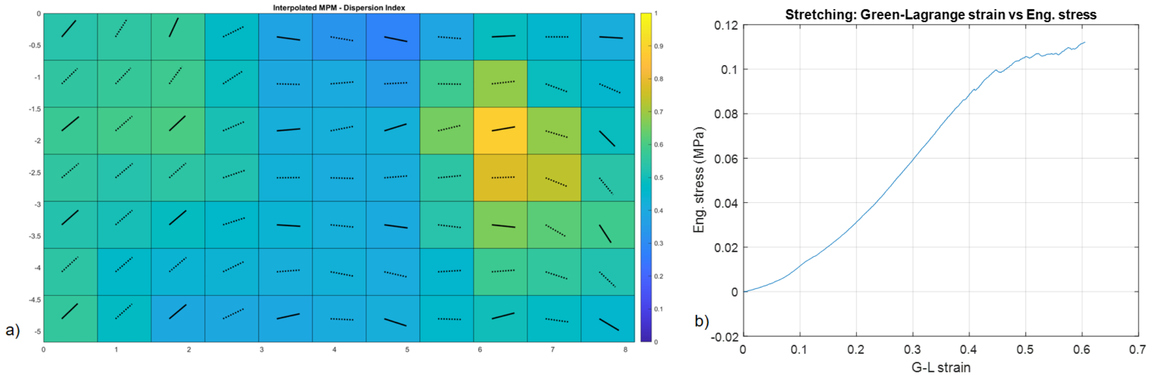

Figure 2.5: Sample B (a) Interpolation Map of Fiber Orientation and Dispersion (b) Engineering Stress-Green-Lagrange Strain [5].

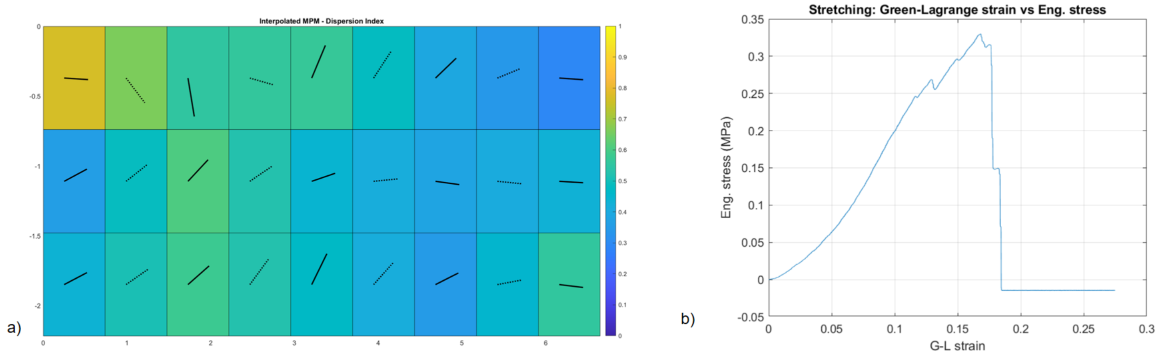

Figure 2.6: Sample C (a) Interpolation Map of Fiber Orientation and Dispersion (b) Engineering Stress-Green-Lagrange Strain [5].

2.1.2. Material Model

Based on the experimental data forming the basis of this research, a phenomenological material model was required. The Holzapfel-Gasser-Ogden (HGO) model was selected due to its widespread use and popularity in the field of tissue biomechanics. HGO model is an anisotropic hyperelastic material model that utilizes a free-energy function, making it particularly well-suited for representing dispersed fiber-reinforced structures [6].

In the HGO model, the isotropic and anisotropic parts of the strain energy function is decomposed as:

$$\Psi = \Psi_{vol} + \Psi_{dev} + \Psi_{ani} \tag{2.2}$$

where

$$\Psi_{vol} = \frac{1}{D}(J-1)^2 \tag{2.3}$$

$$\Psi_{dev} = C_{10}(I_1 - 3) \tag{2.4}$$

$$\Psi_{ani} = \frac{k_1}{2k_2}\left[\exp\left(k_2[\kappa I_1 + (1-3\kappa)I_4) - 1]^2 - 1\right] . \tag{2.5}$$

The first two components are the dilatational (Ψ_{vol}) and deviatoric (Ψ_{dev}) parts of the isotropic response, while the last component represents the contribution of the two families of fibers (Ψ_{ani}). The D value determines the compressibility of the material; when $D = 0$, the material is fully incompressible. J is the Jacobian of the deformation map $F = \frac{\delta x}{\delta X}$. In the second term, C_{10} is the neo-Hookean parameter representing the isotropic matrix of the tissue, and I_1 is the first invariant of the right Cauchy-Green tensor.

The anisotropic component of the strain energy function incorporates several parameters: k_1, a stress-like parameter; k_2, a dimensionless parameter; and κ, a dispersion parameter. Additionally, I_4 is a tensor invariant that represents the square of the stretch along the fiber orientation angle α.

The fiber dispersion κ is defined as

$$\kappa = \int_0^\pi \rho(\Theta) \sin^3(\Theta)\, d\Theta. \tag{2.6}$$

When κ is 0, it represents full fiber alignment, and $\kappa = \frac{1}{3}$ indicates complete dispersion. Figure shows the von Mises distribution of the collagen fiber density with different values of κ.

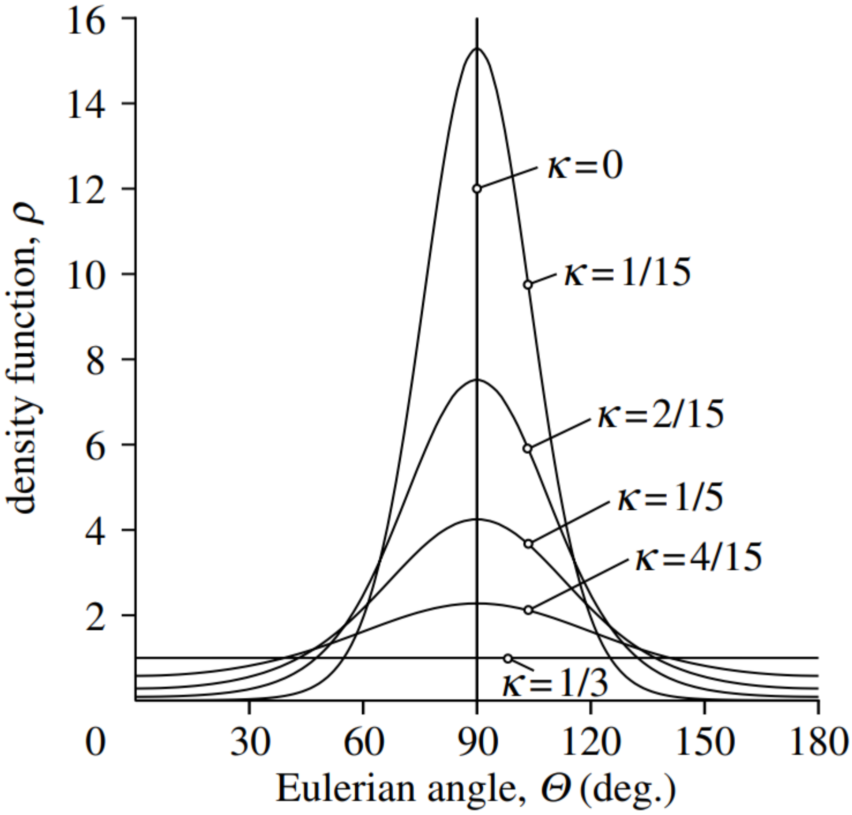

Figure 2.7: Two-dimensional graphical representation of the (transversely isotropic) von Mises distribution of the collagen fibers [6].

2.1.3. Global Material Properties

In the HGO model, five material properties are essential: C_{10}, k_1, k_2, κ, and α. Among these parameters, the first three (C_{10}, k_1, and k_2) are considered global parameters in this research, maintaining consistency throughout the entire sample. These global parameters are crucial in defining the overall isotropic (C_{10}) and anisotropic (k_1 and k_2) mechanical behavior of the material.

The remaining two parameters, κ and α, are considered local parameters, varying in different locations of the sample. κ represents fiber dispersion, indicating the degree of alignment or dispersion of the fibers within the tissue. A higher κ value suggests more dispersed fibers, while a lower value indicates more aligned fibers. α denotes the fiber orientation, specifying the direction of the fibers relative to a reference axis. These local parameters are vital for accurately modeling the anisotropic behavior of the material, as they account for the directional dependence of the tissue's mechanical properties.

As the global material properties are not directly measured in the experiments [5], they are determined through a series of simulations. A MATLAB code is employed to generate one hundred combinations of global parameters, with the condition that C_{10} must be lower than k_1 (Appendix A). With local parameters implemented, the samples are simulated using the 100 parameter combinations. The combination with the closest stress-strain curve to the experimental tensile data is selected. This initial selection is then manually optimized to ensure a more precise fit to the experimental data.

2.1.4. Local Material Properties

As presented in Section 2.1.1, each sample is divided into a grid of tiles, with fiber orientation and dispersion reported for each tile. The fiber orientation, α, is measured relative to the circumferential axis and can be directly implemented in the ABAQUS simulation.

However, while the fiber dispersion index reported from the experiments is DI, the parameter required for the HGO model is κ. There is a relationship between these two parameters that can be utilized to derive κ from DI.

According to Equation 2.6, the first step to obtain κ is to calculate $\rho(\Theta)$ which is

$$\rho(\Theta) = \frac{\bar{\rho}(\Theta)}{I} \tag{2.7}$$

where

$$\bar{\rho}(\Theta) = \frac{\exp(b\cos(2\Theta))}{2\pi I_0(b)} \tag{2.8}$$

and

$$I \equiv \int_0^{\pi} \rho(\Theta) \sin(\Theta)\, d\Theta \equiv \frac{\exp(-b)\,\mathsf{erfi}(\sqrt{2b})}{2\sqrt{2\pi b} I_0(b)}. \tag{2.9}$$

In these equations, $b > 0$ is the concentration parameter associated with the von Mises distribution, and erfi$(x) = -i$erf(x) denotes the imaginary error function [19]. $I_0(x)$ is the modified Bessel function of the first kind of order zero, and integration of the normalization condition gives I [6].

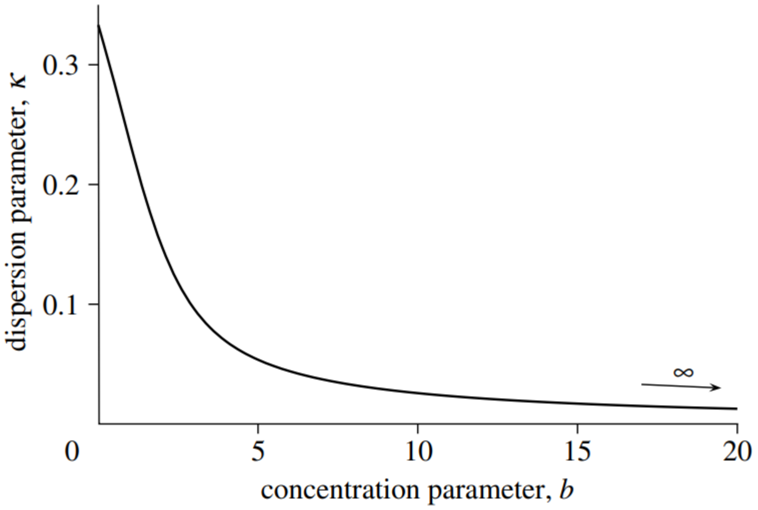

Figure 2.8: Relation between the dispersion parameter κ and the concentration parameter b of the (transversely isotropic) von Mises distribution [6].

The dispersion index (DI) is a function of the standard deviation (σ_p), as reported by de Miguel et al. (2022). The relationship between σ_p and b is given by:

$$\sigma^2 = 1 - \frac{I_1(b)}{I_0(b)} \tag{2.10}$$

where $I_1(x)$ is the modified Bessel function of the first kind of the first order. The parameter b can then be calculated from this equation using a numerical solver. Subsequently, $\rho(\Theta)$ and then κ can be obtained as shown in Equation 2.6. The relation between the dispersion parameter κ and the concentration parameter b is illustrated in Figure 2.8.

A Matlab code is developed to calculate the dispersion parameter of the HGO model from the standard deviation acquired from experimental data (Appendix B).

2.2. Finite Element Analysis

The uniaxial tensile testing of the three CAE samples is simulated using the commercial Finite Element Software ABAQUS/Standard (Dassault Systems). The simulation process involves six general phases: geometry, material model, step settings, boundary conditions, forces, and meshing.

In the first step, the geometry of each sample is replicated in ABAQUS. The CAE samples analyzed in this study are cut in the form of strips and are therefore modeled in ABAQUS with a simplified rectangular geometry based on the dimensions presented in Table 2.1.

To implement the local material properties in a later stage, each sample is partitioned into the number of tiles reported in Figures 2.5 to 2.6. The geometry of Sample B, as an example, is presented in Figure 2.9.

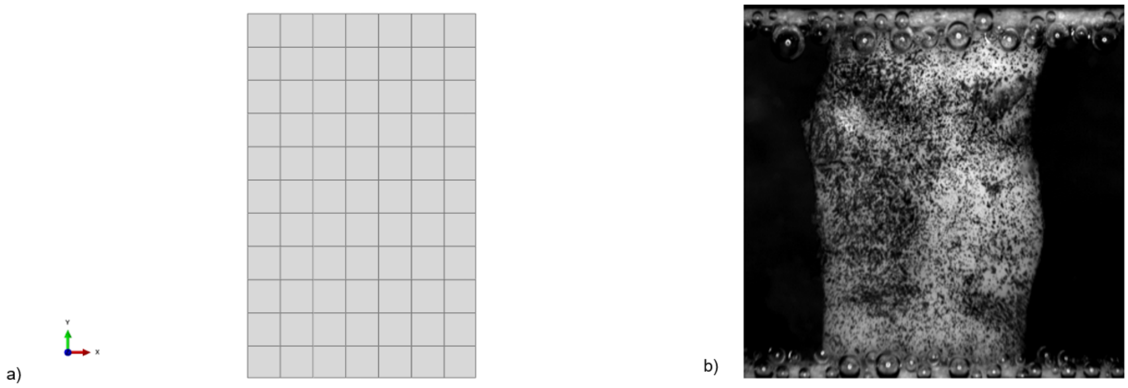

Figure 2.9: Sample B (a) 2D Simulation (b) Experimental Image[5].

Initially, only a 2D geometry is developed for each sample due to the availability of 2D data. This is achieved using a *2D Deformable* part type and a *Solid* section type, with a plane stress thickness equal to the measured experimental thickness (Figure 2.9.a). However, to examine the effect of geometry on the results, a 3D geometry of Sample B is also simulated using a *3D Deformable* part type, as presented in Figure 2.10.

In the next step, each tile is assigned a hyperelastic, anisotropic HGO material model, which requires the parameters C_{10}, D, k_1, k_2, and κ. This material model is natively implemented in ABAQUS. The final material parameter, α, representing fiber orientation, is manually incorporated into the ABAQUS input file for each tile. A detailed representation of this configuration is provided in Figure 2.11.

Subsequently, a *General Static* step is defined in ABAQUS over a time period of 1 second. The dissipated energy fraction is activated as the automatic stabilization, with a standard value of 0.0002, and an adaptive stabilization with a maximum ratio of stabilization to strain energy of 0.05. The incrementation type is set as automatic, and a maximum number of increments is set at 100000, with an initial and maximum step size of 0.01 sec, and a minimum of 1E-08 sec.

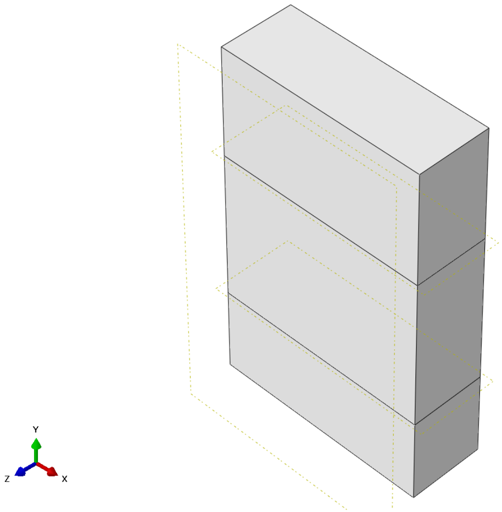

Figure 2.10: Sample B with a 3D geometry with 3 main tiles. More information is provided in the Results chapter.

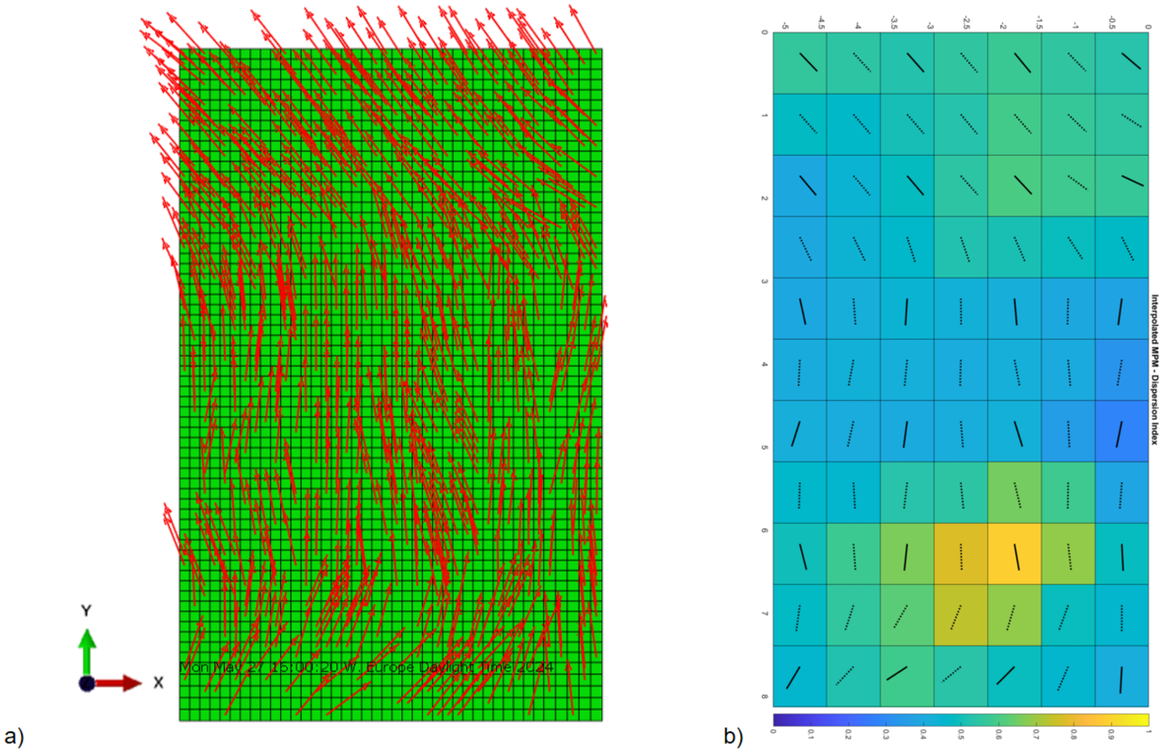

Figure 2.11: Sample B (a) Material Orientation Contour in the Simulation (b) Experimental Data of Fiber Orientation [5]

The fourth stage includes defining boundary conditions and loads. As the experimental tensile tests are displacement-driven, two boundary conditions are assigned to the model. The bottom of each model is constrained in ENCASTRE mode, restricting all transitional and rotational movements of the selected nodes in space. To capture the uniaxial tensile tests, a displacement boundary condition is applied to the top edge of the simulated sample in the Y direction. The magnitude of the displacement varies for each sample and is constrained until the onset of damage. The movement in the X-axis and the rotation around the Z-axis are also constrained at the top edge of the models. The implemented boundary conditions are depicted in Figure 2.12. No external force or pressure is applied to the simulated samples.

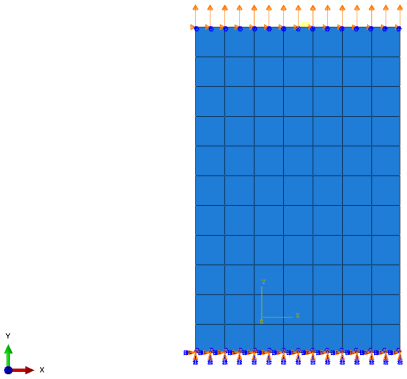

Figure 2.12: Sample B Simulation, Boundary Conditions

The final step of the simulation is meshing, and the element type of CPS4R is chosen for all samples. CPS4R is a 4-node bilinear plane stress quadrilateral, with reduced integration and hourglass control. The approximate global seed size is set to 0.15, and Figure 2.13 shows the meshing configuration.

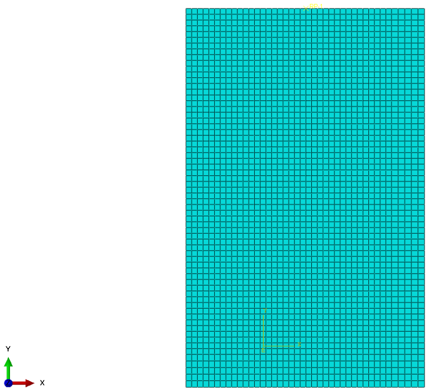

Figure 2.13: Sample B Simulation, Meshing with CPS4R Elements

3

Results

Three samples are modeled and simulated in ABAQUS. The results for each sample are presented in this chapter. One sample is chosen for a parameter study on the effects of local and global material properties on sample deformation.

3.1. Correlation of FEM Simulations with Experimental Data

Three samples are simulated and the global properties that best matched their respective experimental stress-strain curves are determined. Through this process, the optimal parameters are identified for each sample. Figures 3.2 to 3.3 illustrate the results, showcasing both the experimental and computational stress-strain curves for each sample. Moreover, the determined global parameters of the samples are presented in Table 3.1.

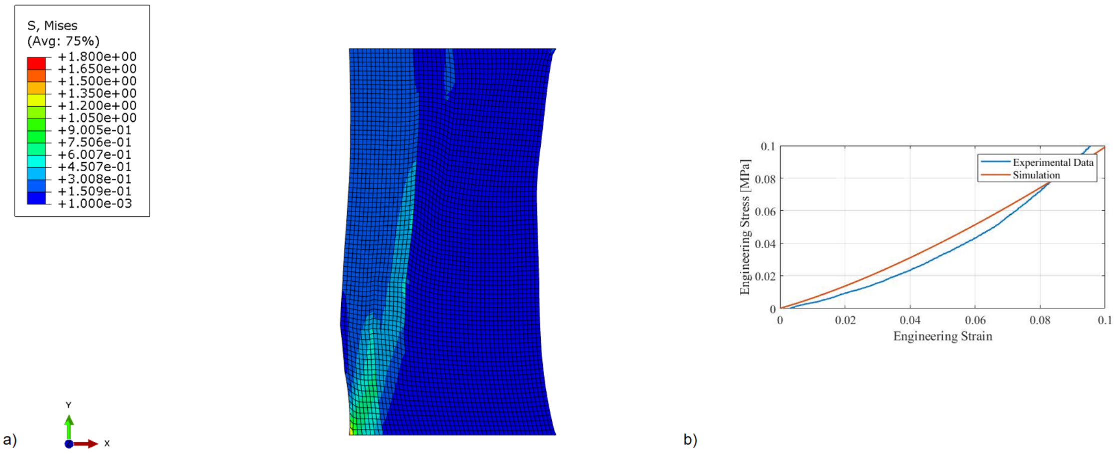

Figure 3.1: (a) FEM Simulation of Sample A (b) Engineering Stress-Strain Curve comparing Experimental and Simulation Results

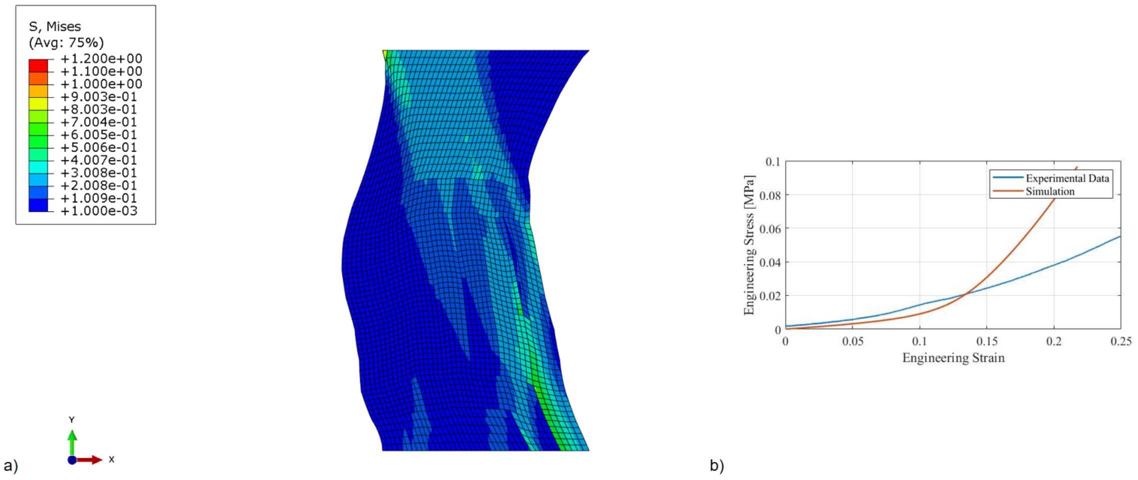

Figure 3.2: (a) FEM Simulation of Sample B (b) Engineering Stress-Strain Curve comparing Experimental and Simulation Results

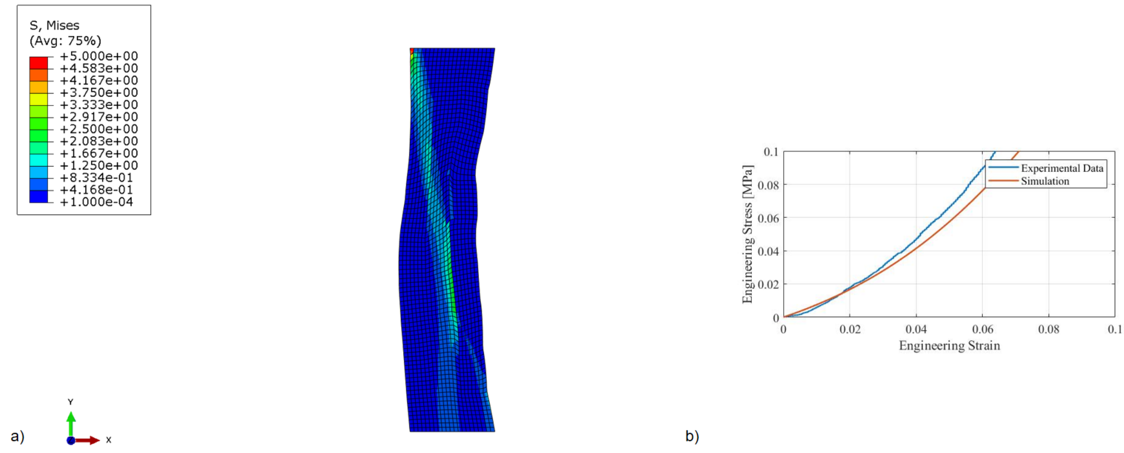

Figure 3.3: (a) FEM Simulation of Sample C (b) Engineering Stress-Strain Curve comparing Experimental and Simulation Results

Table 3.1: Global Material Properties for Samples

Parameter	C_{10} (MPa)	k_1 (MPa)	k_2
Sample A	0.01	1	0.1
Sample B	0.003	1	0.1
Sample C	0.02	5	0.4

To thoroughly investigate the effects of material parameters, Sample B is selected for further examination. This sample is chosen due to the pronounced intensity of its C-shaped deformation, making it an ideal candidate for a detailed analysis of how various material properties influence deformation patterns.

3.2. Parameter Study

The experimental data for sample B consists of local fiber orientation and dispersion across 77 tiles, as illustrated in Figure 2.5. Both the α and κ are implemented in each tile. Using the global material properties provided in Table 3.1, the sample is simulated.

The resulting deformation and stress contour of sample B is depicted in Figure 3.4.

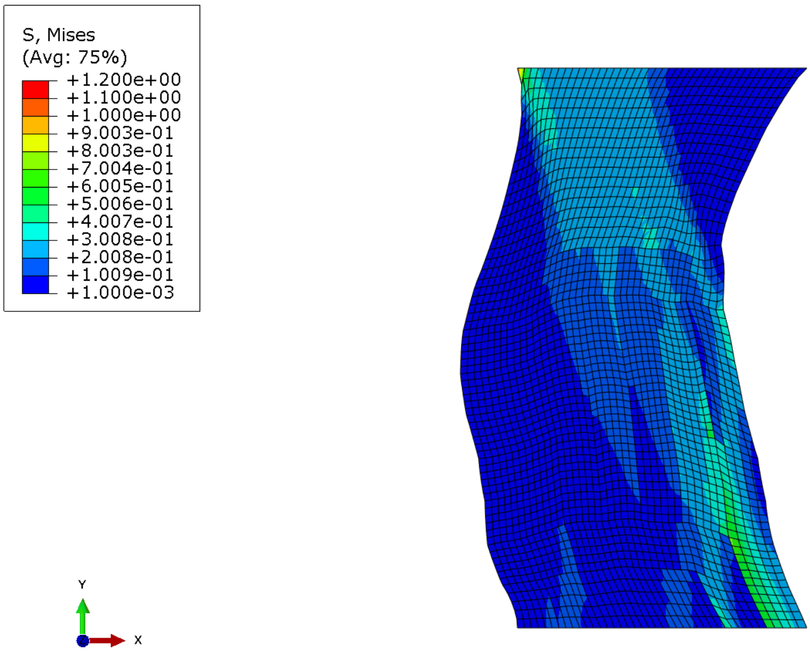

Figure 3.4: Deformation of Sample B and the Mises Stress Contour

The observed deformation differs significantly from the expected behavior as indicated by experimental data. While a predicted expansion in the Y-direction accompanied by a reduction in the X-direction was anticipated, the sample exhibits an irregular C-shaped distortion. Moreover, the sample's centroid experiences a lateral displacement towards the left.

To examine the cause of this deformation, a parameter study is conducted. Initially, the effects of local properties are analyzed by smoothing the variations in local orientation between tiles, followed by a simplification of the sample for further investigation. Subsequently, the magnitude of global material properties and their relative ratios are varied across the entire sample, as well as within different regions of the sample.

3.2.1. Influence of Local Orientation Gradients on Stress and Deformation Patterns

One potential factor contributing to the irregular deformation and stress contour is hypothesized to be the abrupt variation in local material properties from one tile to another. Therefore, the orientation change of fibers between tiles is smoothed to assess whether the discontinuity between different sections is a contributing factor. The sample is subdivided into 231 smaller tiles, with material properties linearly interpolated between adjacent tiles. As depicted in Figure 3.5, these adjustments do not yield significant changes in deformation. However, the abrupt transitions at the partition borders are fully eliminated, resulting in smoother edges for the sample and a more uniform stress contour.

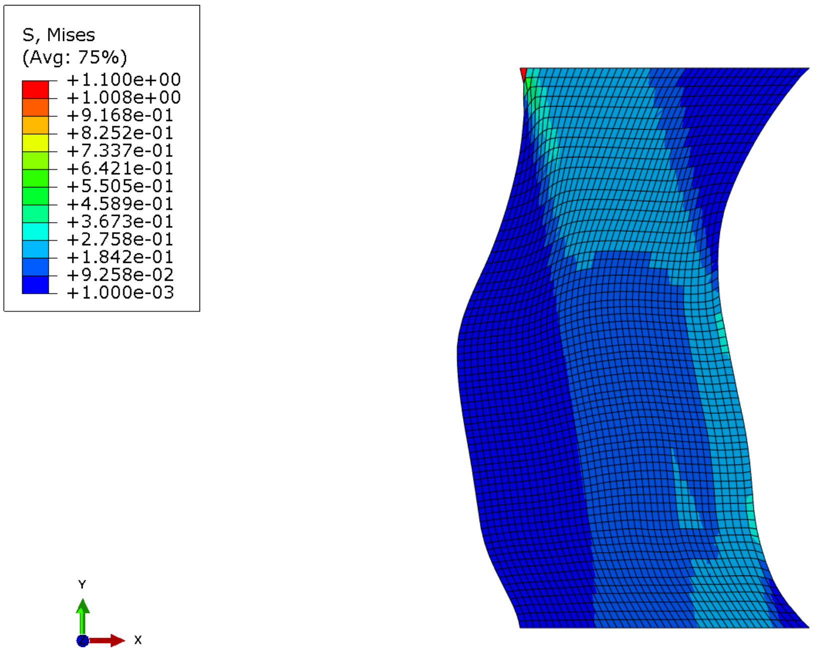

Figure 3.5: Deformation of Sample B and the Mises Stress Contour with Smoothed Local Material Properties

To simplify further investigations, the sample is segmented into three primary regions, each characterized by a predominant fiber orientation, as illustrated in Figure 3.6. In this investigative sample, the lower region exhibits an average orientation of nearly 60 degrees, the middle region has vertical fiber orientation, and the top region shows fibers oriented at approximately 120 degrees. As the focus shifts to examining the effect of different properties on sample deformation, the overall load applied to the sample is limited to a displacement of 1.5 mm to reduce computational time. Furthermore, the global material properties remain constant unless otherwise specified. The result is presented in Figure 3.6.

3.2.2. Evaluating Deformation Consistency in 2D and 3D Models

Subsequently, a 3D model incorporating these segmented material properties is simulated under identical conditions as the 2D model to explore the differences between 2D and 3D models. Despite the change, the irregular bending observed in the 2D simulations persists in the 3D model (Figure 3.7). Recognizing the consistency in deformation patterns between the 2D and 3D models, the remainder of the investigation focuses exclusively on the 2D simulations.

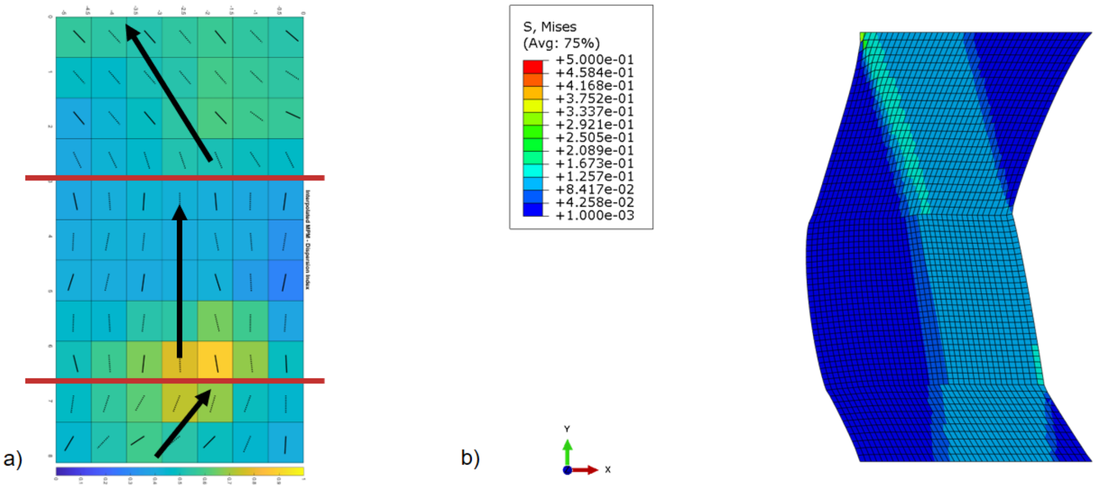

Figure 3.6: Simplification of Sample B (a) a sample with 3 main regions of orientation (b) ABAQUS simulation of this sample

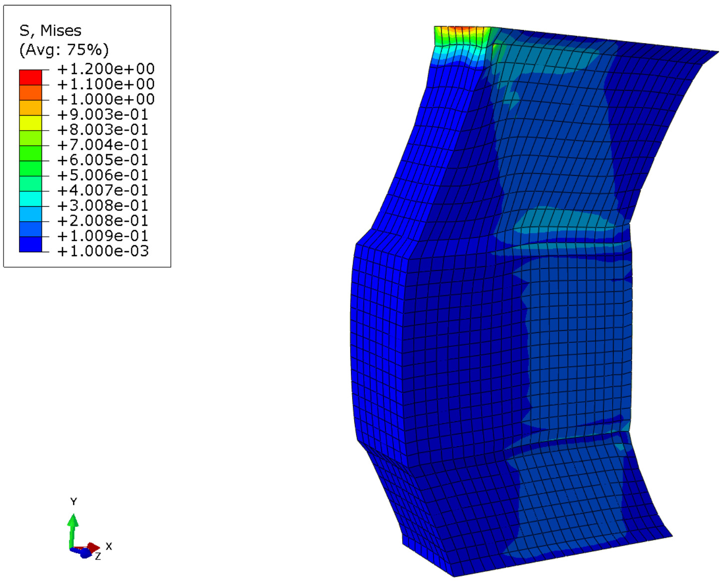

Figure 3.7: 3D Simulation of Sample B with the 3 Main Orientation Regions

3.2.3. Effects of Global Material Properties and k_1 Variations

The next category of investigation focuses on the global material properties, which remained consistent across all elements up to this point of the project. A Matlab code is employed to generate 100 random combinations of these properties, constrained only by the condition that C_{10} must be lower than k_1 (Appendix A). All 100 combinations result in the same irregular bend in the deformation.

To evaluate the impact of global properties in more detail, the assumption of uniformity is abandoned, and different orientation regions are assigned different global properties. Before proceeding, all dispersion parameters are set to 0.2 to isolate the effects of global properties. This setting is maintained consistently throughout the subsequent simulations.

Initially, the k_1 value in the middle region is altered while other parameters are kept consistent as mentioned in Table 3.1. Figure 3.8 illustrates four simulations with varying k_1 values ($k_1 = 10$, $k_1 = 1$, $k_1 = 0.01$ and $k_1 = 0.003$). Higher k_1 values in the region with vertical fiber orientation increase the region's stiffness, thereby reducing the local strain and intensifying the overall deformation shape. Conversely, with lower k_1 values, the middle region exhibits increased stretch, which is most pronounced when $C_{10} = k_1 = 0.003$.

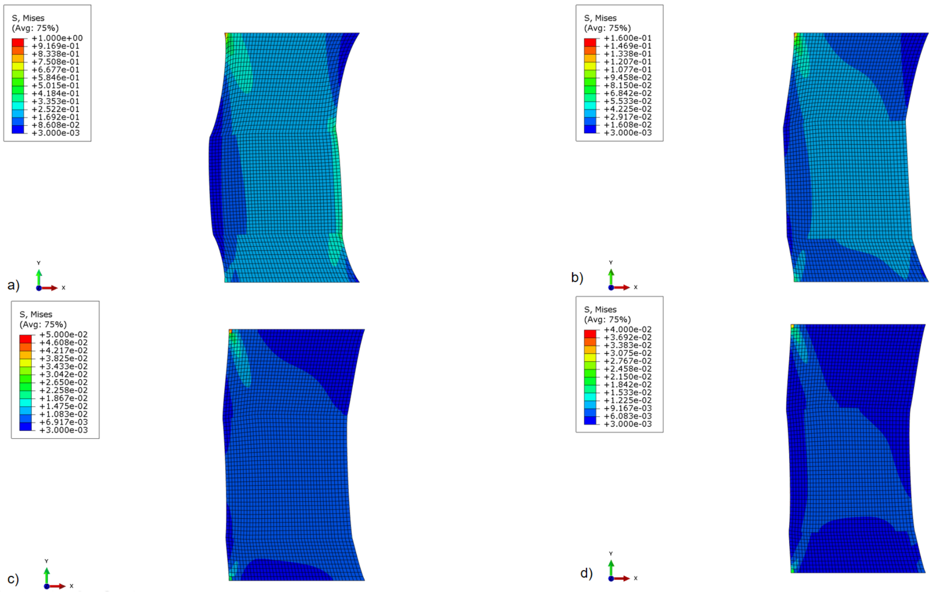

Figure 3.8: Simplified Sample B with Different k_1 Values in the Middle Region (a) $k_1 = 10$ (b) $k_1 = 1$ (c) $k_1 = 0.01$ (d) $k_1 = 0.003$. Note that the contour limits are different in each figure to better display the effect of value change on stress distribution.

Similarly, changing the k_1 value for the lower region produces the same effect; the alteration in k_1 does not impact the lower region's tendency to lean to the left (as shown in Figure 3.9). A similar examination on k_1 is also performed on the upper region, leading to a similar conclusion (Figure 3.10). This consistency across different regions suggests that variations in k_1 alone are insufficient to correct the irregular bending. Therefore, while adjusting k_1 in one region influences local stiffness and strain distribution, it does not significantly alter the global deformation pattern, pointing to the need for further investigation into other factors influencing the irregular deformation.

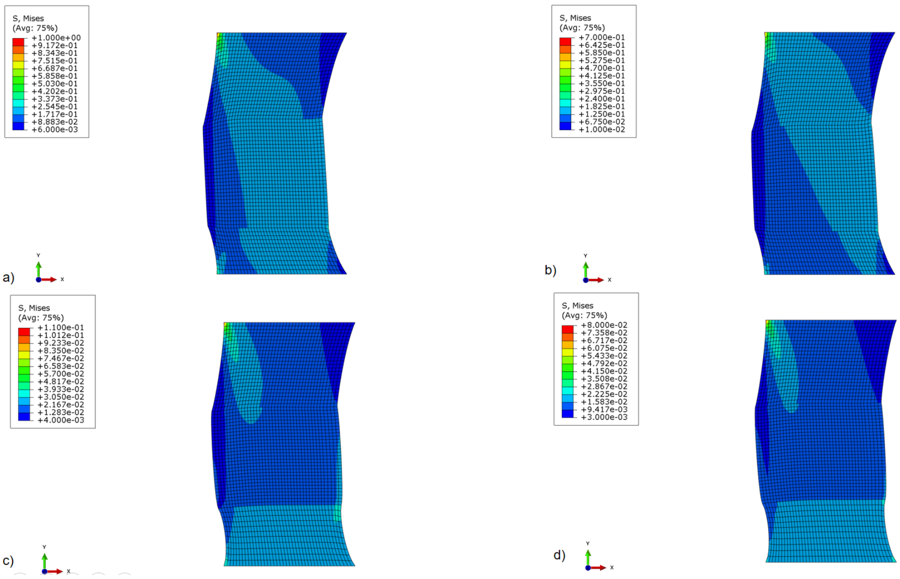

Figure 3.9: Simplified Sample B with Different k_1 Values in the Upper Region (a) $k_1 = 5$ (b) $k_1 = 2$ (c) $k_1 = 0.01$ (d) $k_1 = 0.003$. Note that the contour limits are different in each figure to better display the effect of value change on stress distribution.

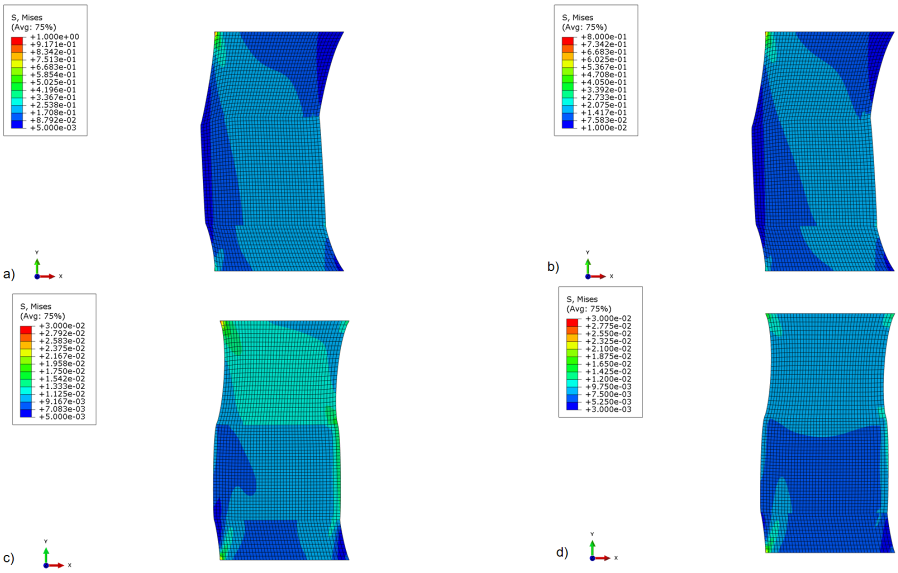

Figure 3.10: Simplified Sample B with Different k_1 Values in the Upper Region (a) $k_1 = 5$ (b) $k_1 = 2$ (c) $k_1 = 0.01$ (d) $k_1 = 0.003$. Note that the contour limits are different in each figure to better display the effect of value change on stress distribution.

3.2.4. Effects of k_2 Variations

Since assigning different global material properties to the regions does not rectify the overall irregular shape, a decision is made to maintain a uniform set of global material properties across the sample. Subsequently, the effect of k_2 is assessed. Figure 3.11 indicates that increasing k_2 throughout the entire sample alters the sample's stiffness but does not affect the deformation pattern. This indicated that changes in k_2 only influence the material's stiffness without addressing the irregular bending observed in the deformation. Therefore, the investigation continues to explore other potential factors contributing to the deformation irregularities.

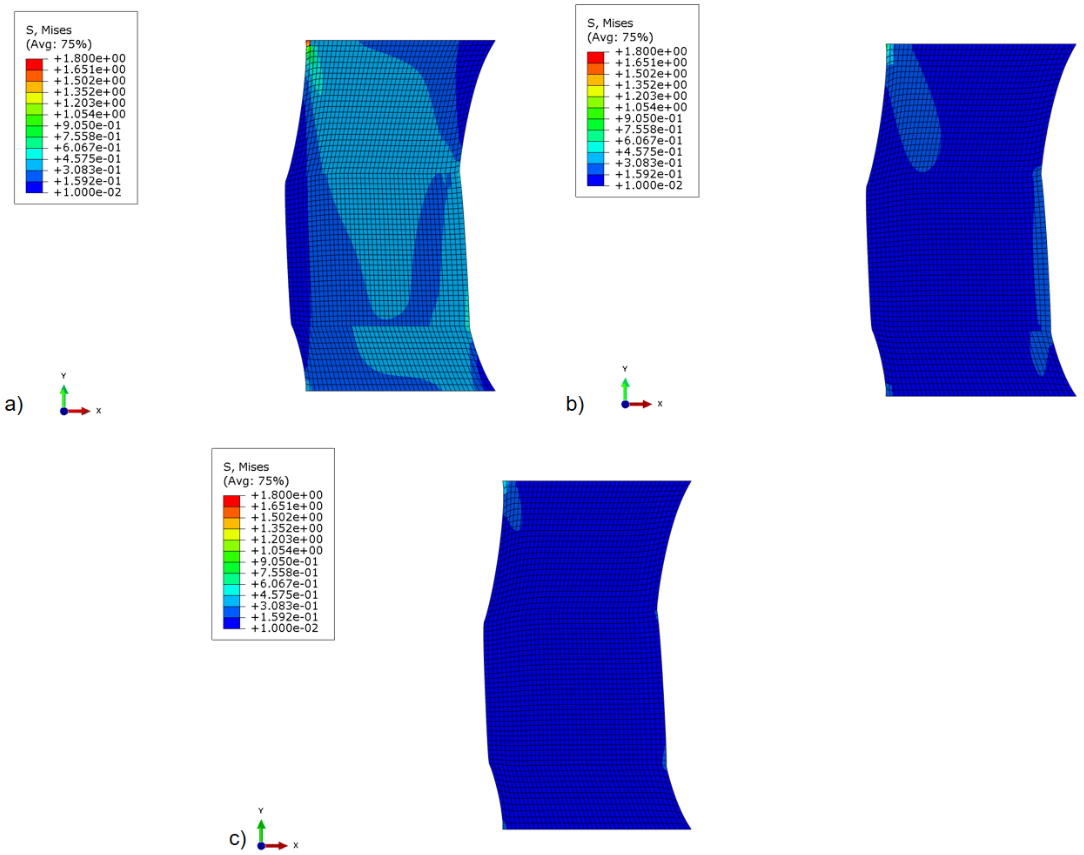

Figure 3.11: Simplified Sample B with Different k_2 Values (a) $k_2 = 100$ (b) $k_2 = 25$ (c) $k_2 = 1$

3.2.5. Effects of k_1 to C_{10} Ratio Variations

The final step in understanding the impact of global material parameters on the deformation involves an investigation of the k_1 to C_{10} ratio. Given that C_{10} and k_1 represent the extracellular matrix stiffness and fiber stiffness respectively, it is hypothesized that their ratio might significantly influence the irregularity of the deformation. A high k_1 to C_{10} ratio indicates that the fibers bear most of the load, which could be a critical factor in the observed deformation patterns.

Figure 3.12 illustrates the effect of varying this ratio on sample deformation. As the k_1 to C_{10} ratio decreases, the severity of the irregular bend also diminishes, reaching its lowest point when C_{10} and k_1 are equal. This suggests that a balanced stiffness between the matrix and the fibers can lead to a more uniform deformation, minimizing irregularities.

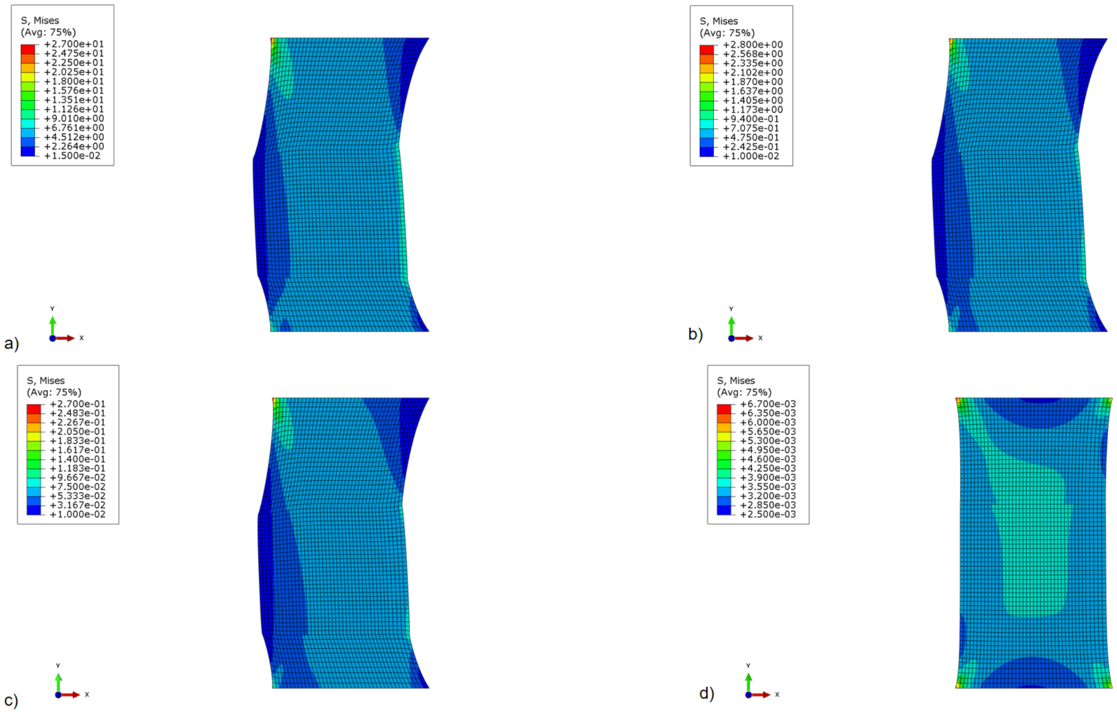

Figure 3.12: Simplified Sample B with Different k_1 to C_{10} Values (a) $C_{10} = 0.003, k_1 = 0.50$ (b) $C_{10} = 0.003, k_1 = 5$ (c) $C_{10} = 0.15, k_1 = 0.5$ (d) $C_{10} = 0.003, k_1 = 0.003$

In the specific case where C_{10} exceeds k_1, the bend is entirely eliminated (Figure 3.13). Although this scenario lacks physical significance for the sample as fibers generally exhibit higher stiffness than the matrix, it provided valuable insights. This simulation demonstrates that the irregular bending can be mitigated by adjusting the relative stiffness of the matrix and the fibers. However, it must be considered that in real-life tissue, fibers exhibit greater stiffness than the surrounding matrix, which means k_1 must be higher than C_{10} for the model to be realistic. Despite the lack of real-life representation, this simulation pronounces the effect of fiber properties on sample deformation.

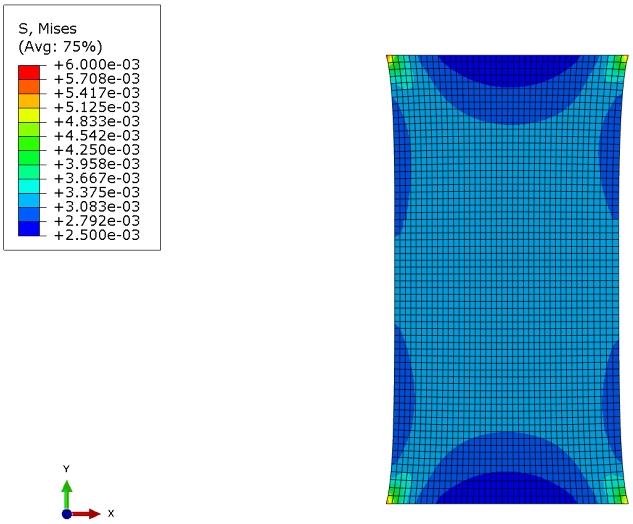

Figure 3.13: Simplified Sample B with $C_{10} = 0.003, k_1 = 0.001$

To further investigate the influence of fibers on the deformation, simulations are conducted with the sample assigned a uniform fiber orientation of 60 degrees and 120 degrees in separate trials. As observed in Figure 3.14 and 3.15, these configurations do not exhibit the irregular bends seen in previous cases. The simulation results, however, are not symmetric and the deformation and stress distribution are highly dependent on the fiber orientations.

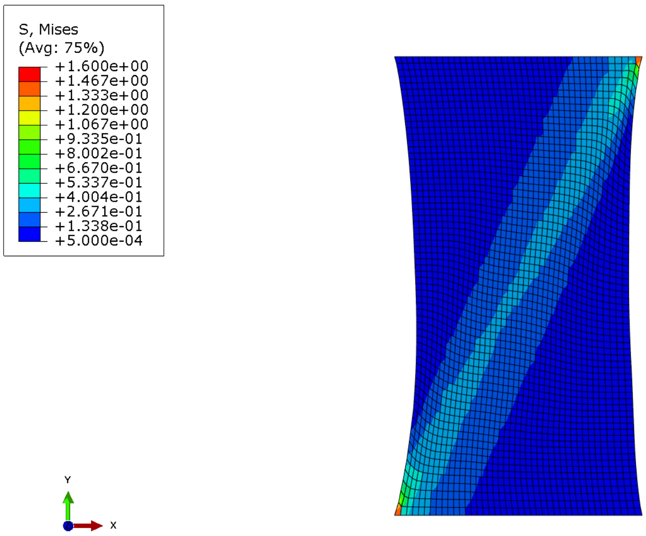

Figure 3.14: Simplified Sample B with Uniform Orientation of 60 degrees

As illustrated in the Mises stress contour figures above, the regions of stress concentration are notably higher along a strip in the direction of the fibers. The absence of bending in the uniformly oriented samples suggests that the interaction between different fiber orientations in the three-region sample plays a crucial role in the deformation behavior.

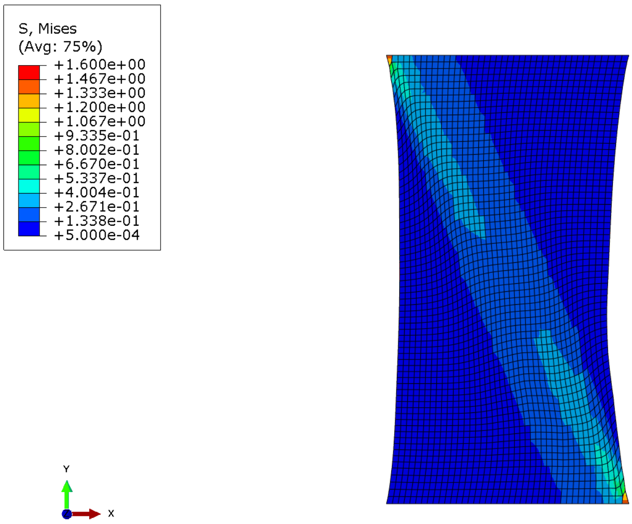

Figure 3.15: Simplified Sample B with Uniform Orientation of 120 degrees

4

Discussion

This chapter provides an in-depth discussion of the Finite Element Model used to analyze atherosclerotic plaques and the simulation results. The first section focuses on an examination of the global material parameters and sample geometry, highlighting key assumptions and their implications. The following sections address observed deformations during simulations, particularly focusing on unexpected irregularities and their potential causes. Finally, the chapter outlines limitations in the experimental data and suggests directions for future research.

4.1. Finite Element Model

4.1.1. Global Material Parameters and Sample Geometry

The CAE strips are modeled in ABAQUS using the HGO material model, which is well-suited for capturing the anisotropic mechanical behavior of soft tissues like atherosclerotic plaques. The material parameters required by this model are categorized into global and local parameters. The global parameters, C_{10}, k_1, and k_2, are initially assumed to be constant across the entire sample. This assumption simplifies the model by maintaining uniformity in certain mechanical properties. However, the plaque tissue is inherently heterogeneous, and local variations could play a significant role in its mechanical behavior. This simplification represents a primary limitation of the FEM model.

Given the absence of direct measurements for these global parameters, a global parameter study is conducted. Initially, 100 random combinations of the global parameters are tested in samples where the local variables, such as collagen fiber orientation and dispersion, are incorporated. The sole constraint on the random generation of these parameters is ensuring that k_1 was higher than C_{10}. The values of k_1 and C_{10} represent the strength of the fiber and the extracellular matrix respectively. Therefore, this constraint suggests that the collagenous component of the strain energy function predominates over the extracellular matrix contribution. Consequently, the collagen network is identified as the primary load-bearing structure within the tissue, a finding in accordance with previous studies [2].

This extensive parameter sweep aims to identify a combination that would best replicate the experimental engineering stress-strain curve. The combination that most closely matched the experimental data is selected as the optimal set of global parameters. Subsequently, a manual optimization process is undertaken to refine this fit further. The manual optimization, while effective, is naturally limited by the precision and subjective judgment of the researcher.

Despite achieving an approximately accurate fit, it is acknowledged that an automated optimization process could significantly enhance the fit and reduce any residual errors. Automated optimization algorithms could systematically explore the parameter space and would not only improve the accuracy of the model but also provide a more robust and objective means of parameter selection.

Moreover, in the process of determining necessary material parameters, each sample is modeled in ABAQUS with local material properties assigned to the geometry. A significant limitation of this study is the inherent simplification of sample geometry. While length, width, and thickness measurements are recorded for each strip, the actual specimens exhibited curvature and deviated from a perfect rectangular shape. To enhance computational efficiency, these complexities are approximated by rectangular models. This geometric idealization may compromise the accuracy of simulation results. The actual shape and curvature of the samples could influence stress and strain distributions, potentially leading to inconsistencies between simulated and experimentally observed mechanical properties.

4.1.2. FEM Analysis of Uniaxial Tensile Tests

After the boundary conditions are applied and the meshing process is completed, the results of the three simulations are subjected to a thorough analysis. Notably, Samples B exhibits an irregular bending deformation in its 2D simulation. Although an expansion in the Y-direction coupled with a reduction in the X-direction was anticipated based on theoretical predictions, the actual behavior of the samples deviates significantly. Instead of the expected deformation pattern, the sample displays an atypical C-shaped distortion, with the centroid of these samples experiencing a lateral displacement towards the left.

The unexpected nature of this deformation necessitates a detailed investigation to uncover the potential causes. Sample B, in particular, is selected for in-depth analysis due to the severity of its bending deformation. Initial efforts focus on addressing the potential issue by smoothing the local fiber orientation, hypothesizing that abrupt property changes between different partitions (tiles) might be contributing to the observed deformation. By implementing a linear interpolation of local orientation among the partitions, sharp transitions in material properties are smoothed. Despite these efforts, as documented in the results section, this change has minimal impact on the C-shape deformation pattern. However, it smooths the stress contour and the sharp bends along the sample's edges.

A more detailed examination of Sample B's local fiber orientation reveals that the sample could be effectively divided into three main regions, each characterized by a predominant fiber orientation. To streamline the simulation process and allocate more focus to the investigative aspects rather than achieving precise real-world replication, each region is assigned a uniform fiber orientation, and all dispersion parameters are set equal. This approach allows for a more focused analysis of the underlying deformation mechanisms without the added complexity of varying fiber orientations and dispersions in each partition.

Following this adjustment, the material parameters are applied to a 3D model to assess whether the deformation observed in the 2D simulations is influenced by the geometry. The results indicate that the shape of the 3D model remains consistent, thus ruling out the 2D geometry as a contributing factor to the observed irregularities.

The next phase of the investigation involves varying the global material parameters across different regions of the sample. This approach aims to explore whether variations in the parameter k_1, which represents fiber strength and can correlate with fiber density, could account for the observed deformation patterns. By decreasing k_1 in the central region of Sample B, where the fiber orientation was predominantly circumferential, a change in deformation is observed. Lowering k_1 reduces the stiffness of this region, leading to increased deformation in the loading direction. Similar changes are noticed when k_1 is reduced in the upper or lower region. However, a new finding emerges by examination of two regions. The deformation and leftward inclination of these two regions exhibit consistent patterns as long as k_1 exceeds C_{10}, a phenomenon that is investigated in greater detail subsequently.

Overall, the study on k_1 highlights the critical role of fiber density in the mechanical response of the CAE samples. This finding underscores the importance of accurately measuring and considering fiber density in future experimental studies.

Given that adjustments to k_1 influences the deformation, it is crucial to analyze the ratio between k_1 and C_{10}. Figure 3.12 illustrates that the intensity of the irregular C-shaped deformation decreases with a lower k_1 to C_{10} ratio. Interestingly, this deformation disappears entirely when k_1 is lower than C_{10}. Figure 3.13 further shows that when the k_1 to C_{10} ratio is less than 1, the sample still exhibits asymmetric Mises stress contours, but the C-shaped deformation is no longer present. This observation suggests that, when the matrix primarily bears the load rather than the fibers, the deformation pattern aligns more closely with the expected behavior of the sample. However, it does not match the nature of tissue in which fibers are the main load bearers, and that is why the ratio of these values was initially constrained in the determination of global parameters. Regardless, these simulation results provide valuable insights into the deformation mechanism, which was primarily influenced by fiber strength and the configuration of the three fiber orientation regions.

Further validation of these fiber effects is obtained by applying a single fiber orientation to the entire sample. This approach allows for direct observation of how asymmetric deformation and stress and strain concentration areas align with the uniform fiber orientation. Such simulations demonstrate that the observed deformation patterns are indeed influenced by the specific fiber orientation configurations, providing further insights into the mechanical behavior of the samples.

Collectively, these observations offer a foundation for comprehending the factors influencing the sample's irregular shape. A detailed explanation of the underlying mechanisms is presented in the following paragraph.

In the simulated Sample B, the lower region is constrained at its bottom edge and features a fiber orientation of 60 degrees relative to the X-axis. Under the uniaxial load, this region tends to align its fibers with the load direction. This alignment causes the upper part of the sample to lean leftward. Similarly, the top region, constrained in the X direction and with a fiber orientation of 120 degrees, causes the lower part of the sample to lean leftward to align its fibers with the Y-axis, the direction of the applied load. However, in the middle region, where the fibers are initially aligned with the loading direction, the deformation primarily manifested as elongation in the Y-direction. Despite this, the presence of lateral displacement in the upper and lower edges of the region, which lean to the left, results in a transition of the middle region that resembles the behavior of a rigid body movement. This rigid body-like lateral shift occurs because the middle section, although elongated as expected, also experiences a net lateral movement consistent with the deformation observed in the adjacent regions.

This behavior is illustrated in the schematic Figure 4.1, which depicts the changes in fiber orientation under uniaxial loading conditions.

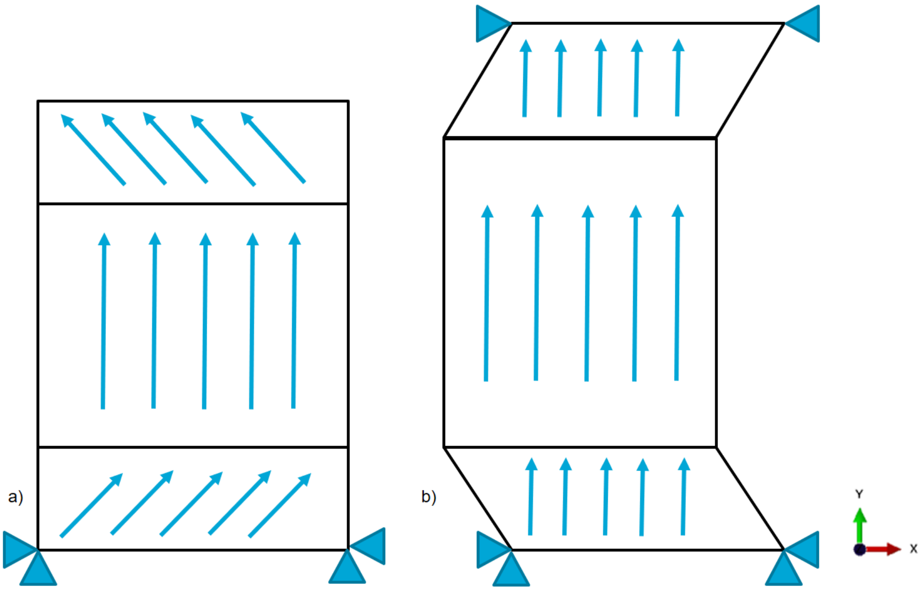

Figure 4.1: Schematic Sketch of a Simplified Sample B (a) Undeformed (b) After Deformation

The abnormal C-shape deformation can also be partially observed in the other samples. The orientation map of Sample A shows two main parts in terms of fiber angle configuration: one region similar to Sample B and the other with a nearly uniform fiber orientation of around 60 degrees. The region similar to Sample B is outlined in Figure 4.2, and the deformation pattern in the left part of this sample matches the observations of the Sample B parameter study.

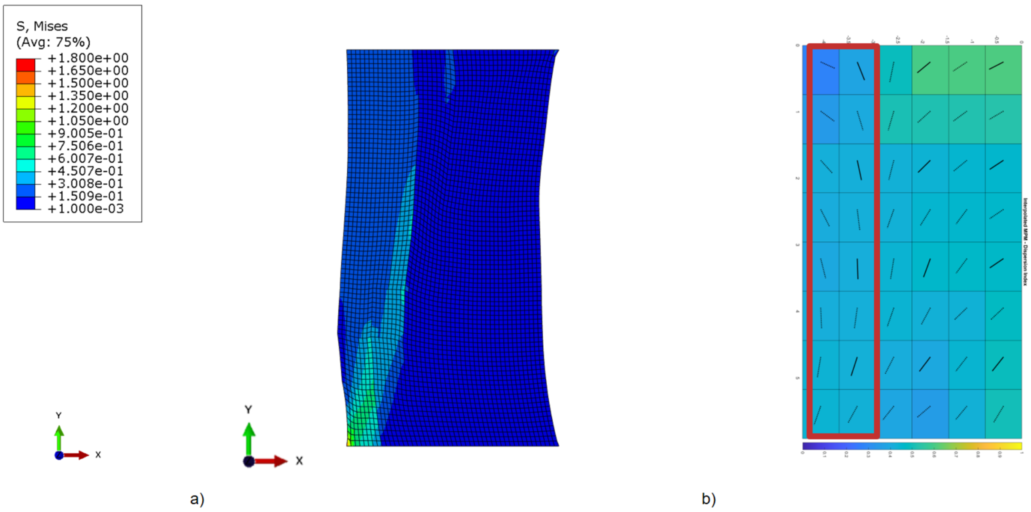

Figure 4.2: Sample A (a) ABAQUS Simulation (b) Experimental Deformation Map [5]

A similar observation is noticed in Sample C, however, the right part of the sample shows a random distribution of fiber orientations. Interestingly, in both samples, the region similar to Sample B shows a higher stress concentration, which requires further investigation in future research.

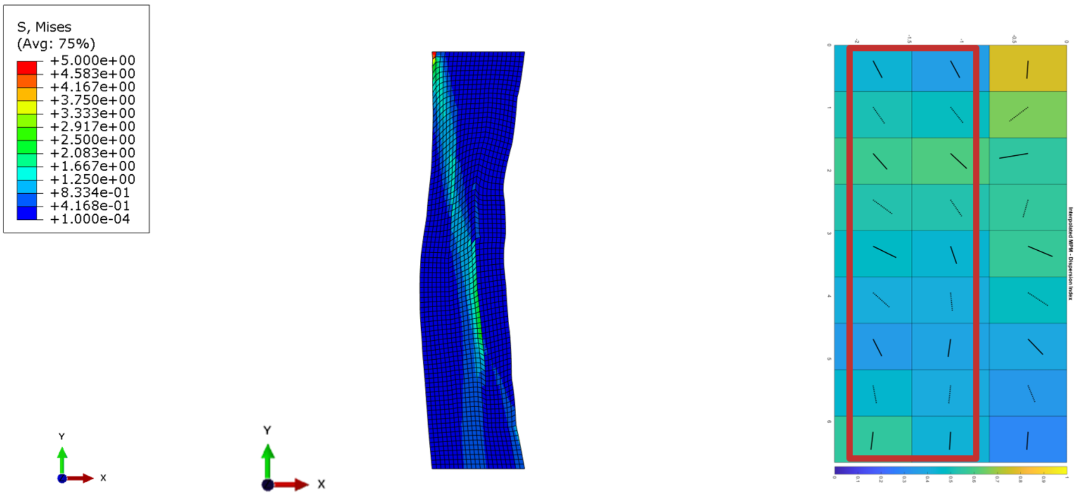

a) b)

Figure 4.3: Sample C (a) ABAQUS Simulation (b) Experimental Deformation Map [5]

4.2. Experimental Data Limitations

The integration of experimental data into finite element models for atherosclerotic plaques has offered significant potential for understanding plaque mechanics. However, several limitations of the dataset must be carefully considered.

A fundamental limitation is related to the characterization of collagen fiber microstructure. MPM imaging provides valuable data but is restricted to low imaging depths. This limits the ability to capture the full complexity of fiber orientation and dispersion throughout the plaque's thickness. Moreover, the assumption of uniform fiber properties across the plaque depth is a simplification that may not accurately represent the heterogeneous nature of these structures.

The methodology employed to image collagen fibers is also coupled with uncertainties. Due to the long imaging times, not the entire test samples but only selected regions in the samples are imaged (approximately 40% of the total sample area), and values for the remaining areas are interpolated linearly [5]. The interpolation of fiber properties between measured sections might oversimplify the complex spatial distribution of fibers within the plaque. A more accurate representation of fiber arrangement would require more comprehensive spatial data.

Another critical aspect concerned the quantification of fiber density. No collagen density is measured in the experiments. However, an investigation on different k_1 values, corresponding to different fiber densities, shows the significant effect of this variable in sample deformation, and stress distribution. The lack of information on collagen fiber density limited the model's predictive capabilities as the true impact of density on plaque mechanics remains uncertain.

Moreover, the simulation utilized an average thickness value for the plaques, overlooking potential local variations in thickness. Atherosclerotic plaques can exhibit significant heterogeneity in thickness across different regions, which can impact their overall mechanical response. By neglecting these local variations, the simulation may oversimplify the plaque geometry, potentially leading to discrepancies between the model's predictions and actual behavior under load.

Finally, the omission of viscosity in the model represents another potential source of error. Viscoelastic properties influence plaque behavior, especially under dynamic loading conditions. Neglecting viscosity may lead to an oversimplified representation of plaque mechanics.

4.3. Suggestions

Future research should include several key areas. Initially, a comparative assessment of alternative hyperelastic anisotropic material models is necessary to determine their suitability for simulating local fiber orientation and dispersion in soft, fibrous tissues similar to atherosclerotic plaque. Simultaneously, addressing the present study's limitations, such as geometric simplifications and manual parameter optimization, is crucial to enhance model robustness.

Moreover, developing advanced techniques for comprehensively characterizing fiber microstructure, including depth-resolved measurements and image analysis, is essential. Additionally, direct measurement of fiber density and incorporation of viscoelastic properties will augment model fidelity. Lastly, considering the influence of local thickness variations on plaque mechanics is important for achieving a more accurate representation of plaque behavior. By systematically addressing these aspects, future models can provide more robust insights into plaque mechanics.

5

Conclusion

5.1. Concluding Remarks

This study investigated the mechanical behavior of atherosclerotic plaque strips through comprehensive FEM simulations and parameter studies. Three plaque samples were chosen and then modeled using the HGO material framework, focusing on accurately capturing the local fiber properties of plaque tissues.

Unexpected C-shaped deformations in the simulations highlighted the need to consider a deeper study of material properties, resulting in a series of investigations. These investigations included an examination of material parameters' effects on sample deformation and showed that regional differences in fiber orientation and density significantly influence the mechanical response of the plaques. These findings underscore the necessity of incorporating detailed local material characteristics into FEM simulations to enhance predictive accuracy.

Additionally, this work identified several limitations in the current experimental data, such as the interpolation of fiber properties and the omission of fiber density and local thickness variations.

Overall, this research provided a foundational understanding of the factors affecting plaque mechanics and offers valuable insights for future studies aimed at improving the accuracy and applicability of FEM models in cardiovascular research.

References

[1] A. C. Akyildiz and et al. "3D fiber orientation in atherosclerotic carotid plaques". In: *Journal of Structural Biology* 200.1 (2017), pp. 28–35.

[2] A. C. Akyildiz, L. Speelman, and F. J. Gijsen. "Mechanical properties of human atherosclerotic intima tissue". In: *Journal of Biomechanics* 47.4 (2014), pp. 773–783.

[3] Britannica, The Editors of Encyclopaedia. *atherosclerosis*. Accessed: 2024-07-25. July 2024. URL: `https://www.britannica.com/science/atherosclerosis`.

[4] H. Crielaard et al. "A Method to Study the Correlation Between Local Collagen Structure and Mechanical Properties of Atherosclerotic Plaque Fibrous Tissue". In: *Journal of Visualized Experiments* (189) (2022), e64334. DOI: `10.3791/64334`.

[5] P. De Miguel Muñoz. "Global and local analysis of the mechanical and structural characteristics of carotid atherosclerotic plaques for rupture risk assessment". © 2022 Pablo De Miguel Muñoz. Master's thesis. Delft University of Technology, 2022.

[6] T. Christian Gasser, Ray W. Ogden, and Gerhard A. Holzapfel. "Hyperelastic modelling of arterial layers with distributed collagen fibre orientations". In: *Journal of the Royal Society, Interface* 3.6 (2006), pp. 15–35. DOI: `10.1098/rsif.2005.0073`.

[7] G. A. Holzapfel, G. Sommer, and P. Regitnig. "Anisotropic mechanical properties of tissue components in human atherosclerotic plaques". In: *Journal of Biomechanical Engineering* 126.5 (2004), pp. 657–665.

[8] Gerhard Holzapfel. "Biomechanics of Soft Tissue". In: *The Handbook of Materials Behavior Models* 3 (Dec. 2001), pp. 1049–1063. DOI: `10.1016/B978-012443341-0/50107-1`.

[9] Gerhard Holzapfel and Behrooz Fereidoonnezhad. "Modeling of Damage in Soft Biological Tissues". In: Dec. 2017, pp. 101–123. ISBN: 9780128040096. DOI: `10.1016/B978-0-12-804009-6.00005-5`.

[10] Gerhard A. Holzapfel, Gerhard Sommer, and Peter Regitnig. "Anisotropic Mechanical Properties of Tissue Components in Human Atherosclerotic Plaques ". In: *Journal of Biomechanical Engineering* 126.5 (Nov. 2004), pp. 657–665. ISSN: 0148-0731. DOI: `10.1115/1.1800557`. eprint: `https://asmedigitalcollection.asme.org/biomechanical/article-pdf/126/5/657/5768634/657\_1.pdf`. URL: `https://doi.org/10.1115/1.1800557`.

[11] R. D. Johnston, R. T. Gaul, and C. Lally. "An investigation into the critical role of fibre orientation in the ultimate tensile strength and stiffness of human carotid plaque caps". In: *Acta Biomaterialia* 124 (2021), pp. 291–300.

[12] C. L. Lendon et al. “Testing of small connective tissue specimens for the determination of the mechanical behaviour of atherosclerotic plaques”. In: *Journal of Biomedical Engineering* 15.1 (1993), pp. 27–33.

[13] H. M. Loree et al. “Static circumferential tangential modulus of human atherosclerotic tissue”. In: *Journal of Biomechanics* 27.2 (1994), pp. 195–204.

[14] E. Maher and et al. “Tensile and compressive properties of fresh human carotid atherosclerotic plaques”. In: *Journal of Biomechanics* 42.16 (2009), pp. 2760–2767.

[15] Johns Hopkins Medicine. *Atherosclerosis*. Accessed: 2024-07-22. n.d. URL: `https://www.hopkinsmedicine.org/health/conditions-and-diseases/atherosclerosis`.

[16] R. Pahwa and I. Jialal. *Atherosclerosis*. StatPearls [Internet]. Updated 2023 Aug 8. Treasure Island (FL): StatPearls Publishing, 2023. URL: `https://www.ncbi.nlm.nih.gov/books/NBK507799/`.

[17] Z. Teng and et al. “A uni-extension study on the ultimate material strength and extreme extensibility of atherosclerotic tissue in human carotid plaques”. In: *Journal of Biomechanics* 48.14 (2015), pp. 3859–3867.

[18] Su Guvenir Torun et al. “Local characterization of collagen architecture and mechanical failure properties of fibrous plaque tissue of atherosclerotic human carotid arteries”. In: *Acta Biomaterialia* 164 (2023), pp. 293–302. ISSN: 1742-7061. DOI: `https://doi.org/10.1016/j.actbio.2023.04.022`. URL: `https://www.sciencedirect.com/science/article/pii/S1742706123002143`.

[19] Eric W. Weisstein. *Erfi*. MathWorld – A Wolfram Web Resource. `http://mathworld.wolfram.com/Erfi.html`. 2005.

A

Appendix A: Global Material Properties

The following MATLAB Code was used to generate a hundred random combinations of global material properties.

```matlab
% Define the ranges and create lists of rounded values
C10_values = [0.05, 0.1, 0.5, 1, 5, 10, 25, 50];
K1_values = [1, 5, 10, 20, 50, 75, 100];
K2_values = [5, 10, 50, 100, 500, 1000, 1500, 2000, 2500];

% Number of combinations
num_combinations = 100;

% Initialize combinations array
combinations = zeros(num_combinations, 3);

% Set random seed for reproducibility
rng(0);

for i = 1:num_combinations
    while true
        % Randomly sample values for C10, K1, and K2
        C10_value = C10_values(randi(length(C10_values)));
        K1_value = K1_values(randi(length(K1_values)));
        K2_value = K2_values(randi(length(K2_values)));

        % Check constraint C10 < K1
        if C10_value < K1_value
            combinations(i, :) = [C10_value, K1_value, K2_value];
            break;
        end
    end
end
```

B

Appendix B: Dispersion Index

The following MATLAB Code was used to calculate κ from the experimental Dispersion Index.

```
    % Define a tolerance for the solution
    tol = 1e-2;
    SD_int1 = SD_int(1:6,1:8);
    % Convert degrees to radians
    sigma = deg2rad(SD_int1);

    % Initialize kappa matrix with zeros
    kappa_mat = zeros(size(SD_int1));

    % Loop through each element of SD_int
    for i = 1:size(SD_int1, 1)
        for j = 1:size(SD_int1, 2)
            % Initial guess for b (can be adjusted if needed)
            b_guess = 2.5;

            % Define the function to be solved (f(b))
            f = @(b) sqrt(1 - besseli(1, b) / besseli(0, b)) - sigma(i, j);

            % Use a numerical solver (fsolve) to find the root of f(b)
            b = fsolve(f, b_guess, optimset('TolX', tol));

            % Define the function rho(theta) using the computed b
            rho = @(theta) (4 * sqrt(b / (2 * pi))) * exp(b * (cos(2*theta) + 1))
                ./ erfi(sqrt(2*b));

            % Define the integrand function
            integrand = @(theta) rho(theta).*(sin(theta)).^3;

            % Calculate the integral from 0 to pi
            kappa_mat(i, j) = 1/4 * integral(integrand, 0, pi);
        end
    end
save(kappa_mat.mat, 'matrix');
```